Robotica (2025), **43**, pp. 1608–1639
doi:10.1017/S0263574725000542

CAMBRIDGE UNIVERSITY PRESS

RESEARCH ARTICLE

Overcoming obstacles with variable geometry and inclination by rolling mobile robots using their arm

Jesús Marcey García and Franklyn Duarte

Laboratorio de Prototipos, Universidad Nacional Experimental del Táchira, San Cristóbal, Venezuela
Corresponding author: Jesús Marcey García; Email: jmgarcia@unet.edu.ve

Received: 9 August 2024; **Accepted:** 24 March 2025; **First published online:** 19 May 2025

Keywords: rolling mobile robots; overcoming obstacles; fuzzy logic; navigability; tip-over stability; motion control

Abstract

Outdoor mobile robots must navigate uneven terrains with obstacles that sometimes cannot be avoided; therefore, strategies have been developed for robots to overcome them. In most cases, these strategies have been modeled considering movement over horizontal surfaces and with the robot positioned directly in front of the obstacle, but this idealization does not occur in most real cases. Therefore, this article describes a strategy for obstacle overcoming, useful when the robot faces obstacles on inclined terrains and at an oblique angle relative to the robot's trajectory, considering rollover stability during the process, based on the reaction force criterion. This strategy can be used by mobile robots with wheels and an articulated arm whose end effector can contact the ground, and it consists of a sequence of standard movements that include the use of the arm, whose variable location was defined through a system developed using fuzzy logic. The designed strategy was validated through simulations and then implemented on the Lázaro robot, verifying its effectiveness through experimental tests. With it, the robot can overcome obstacles such as steps, ramps, and ditches from any position; additionally, it increased the ability to overcome obstacles with a height close to twice the radius of the robot's wheels.

1. Introduction

The deployment of field mobile robots has expanded in recent years, supporting tasks like mining, exploration in hazardous environments, demining, surveillance, search and rescue, inspection, fruit harvesting, firefighting, and cargo transport. To achieve these functions, several challenges have been addressed: designing robust locomotion systems for safe movement, optimizing energy sources for autonomy, developing intelligent control methods for precise navigation, and implementing evaluation strategies to ensure safe terrain traversal. The latter includes assessing rollover and sliding risks [1], minimizing these hazards, and overcoming unavoidable obstacles through trajectory planning.

Overcoming obstacles remains a significant challenge for researchers. While the literature highlights various technological advancements, many are limited to controlled environments that are far simpler than real-world terrains with highly irregular surfaces [2, 3]. Additionally, there is a critical need for more efficient technologies to navigate obstacle-laden terrains, especially in contexts like planetary exploration [4] (e.g., Mars missions). The failure of a robot [5] or its inability to complete expected tasks [6] in such challenging terrains could result in multimillion-dollar losses.

In this regard, the study of obstacle overcoming encompasses two main research areas: the design of robots equipped with mechanisms tailored to overcome obstacles within specific design parameters, and the development of strategies that enable a single mechanical system to address obstacles through various approaches. These areas are interdependent, as a robot's design often aligns with the intended strategy, while the success of any strategy depends on the robot's mechanical characteristics. Numerous wheeled robotic systems have been developed by combining diverse designs and strategies to improve obstacle-handling efficiency. These include robots with active [7] and passive [8] suspension systems,

© The Author(s), 2025. Published by Cambridge University Press.

https://doi.org/10.1017/S0263574725000542 Published online by Cambridge University Press



Figure 1. *Lázaro robot.*

such as *rovers* using the *Rocker-Bogie* mechanism [9–11], rotational wheel structures [12], wheels with appendages [13], segmented wheels [14], transformable wheels [15], and wheels with mounted supports [16]. Other innovations involve robots with multiple tracks [17], some of which are reconfigurable [18], and robots integrating multiple locomotion systems: legged systems for walking [19] or jumping [20] over obstacles, combinations of legs and wheels for rolling or walking independently [21], legs with tracks [22], legs and tracks [23], and systems integrating legs, wheels, and tracks independently [24]. Additionally, robots with modular attachments [25] enable sequential obstacle navigation, while others use supplementary links or arms [26] for added support during traversal. In the case of wheeled mobile robots designed to overcome obstacles, they typically employ strategies based on a common simplification: the robot is assumed to approach obstacles on horizontal terrain, facing them head-on at a 90° angle relative to its trajectory. While this assumption is valid in many scenarios, it diverges from more realistic conditions where robots may navigate inclined terrain or encounter obstacles at oblique angles. On inclined terrain, the robot often lacks viable solutions to address the challenge, whereas for oblique obstacles, it could reorient itself to face them directly. However, such trajectory adjustments may, in some cases, prove counterproductive.

Therefore, it is necessary to develop strategies that allow these types of robots to overcome obstacles considering a more realistic environment, with inclined terrains and obstacles located in any orientation relative to the robot's posture. In this sense, this project aimed to develop, validate, and test a new strategy for overcoming obstacles regardless of the inclination of the obstacle and its orientation concerning the robot's trajectory, considering tipover stability, as the robot can become unusable due to a rollover phenomenon during this operation. This strategy is designed to be used by wheeled mobile robots equipped with an articulated arm and an end-effector that allows rolling or sliding contact with the ground. For its validation, a task planner was developed and implemented in Lázaro (Figure 1), which is a wheeled mobile robot equipped with an articulated arm with a wheel as the end-effector [27].

1.1. Contributions

The main contributions of this work are threefold: first, the design, validation, and implementation of a new strategy for overcoming obstacles formed by inclined surfaces. In this regard, the developed strategy has some particularities: (a) the arm is used as support to achieve the overcoming of obstacles,

https://doi.org/10.1017/S0263574725000542 Published online by Cambridge University Press

positioning it in different predefined positions through a fuzzy inference system based on the inclination of the obstacle and the orientation of the robot relative to the obstacle (unlike other analogous strategies, where the arm is always placed either in front of or behind the robot [26, 28, 29]); (b) the ability to overcome obstacles by positioning the robot in any orientation relative to the obstacle (as opposed to analogous strategies where the robot must be oriented head-on toward the obstacle to overcome it); c) the capability to use either a pair of side wheels or front wheels to surpass the obstacle (depending on the robot's orientation relative to the obstacle), compared to other strategies designed to use only the front (and rear) pair of wheels for this purpose. These features allow for defining a versatile strategy that can be used to overcome multiple obstacles formed by inclined surfaces, while the robot faces them from any orientation.

The second contribution is the modeling of the reaction forces of the wheels with the inclined ground in all stages of the overcoming strategy, including those moments when some wheels do not touch the ground or when involuntary rotations occur in the robot due to the obstacle's terrain. Finally, an analysis of tipover propensity using a quantitative metric based on reaction forces allows for estimating the tipover risk, considering that at various moments, some wheels do not touch the ground, increasing the robot's instability.

2. Initial considerations

2.1. Premises

Initially, some guiding principles were defined to delimit and address the problem considering certain simplifications:

a. The deliberative paradigm was employed in defining the strategy: when the robot encounters the obstacle, it evaluates the dimensional requirements beforehand and outlines all the actions it must take to overcome the obstacle while maintaining the tip-over stability. Subsequently, the overcoming process is executed.
b. The designed strategy does not involve a change in the robot's orientation relative to the obstacle during the overcoming process.
c. The four contact points of the wheels with the ground are located in the same plane. This implies that both the suspension effect and the flexibility of the robot's parts are considered negligible.
d. Each wheel contact with the terrain is assumed to be point-like, understanding that the wheels are considered rigid.
e. During the execution of the strategy by the robot, a set of real-time evaluated parameters are acquired through sensors installed on the robot.
f. The strategy was defined according to a quasi-static analysis, which can be implemented when the robot and its manipulator move at low speeds and there are no significant accelerations or inertial components apart from gravity, nor major external loads [30, 31]. Therefore, the effect of dynamic loads was not considered.
g. Preliminary characterization of the obstacle: basic geometric information of the obstacle (set of characteristic points) will be necessary to define its components, simplifying them as planes and straight lines. It is worth noting that obtaining such information is not part of the purpose of this work; it is considered known, derived from some characterization system, preferably using LiDAR [26].

2.2. Characterization of the robot's geometry

For this study, Lázaro [27] was used (Figure 1), a *skid steer* robot with four wheels, weighing 255.1 N, and equipped with an attached arm (weighing 36.9 N) that has two degrees of freedom: one rotational (θ_1) that moves the first link of the arm, and one prismatic (d_2) that moves the second (Figure 2a). The ranges

https://doi.org/10.1017/S0263574725000542 Published online by Cambridge University Press

of these joint variables are: $-180° \leq \theta_1 \leq 180°$ (without rotation limit) and $-432.5 \leq d_2 \leq -132.5$ mm. These magnitudes can be estimated using an absolute encoder and a potentiometer installed in the two arm joints. Additionally, the end-effector of the arm is a caster wheel with an installed sensor that allows estimating the magnitude of the contact force of this wheel with the ground. The maximum speed reached by the vehicle moving in a straight line is 280 mm/s and can be estimated by the encoders installed in the two drive motors (left and right), which also allow obtaining approximate odometry. Finally, the robot has an Inertial Measurement Unit (*IMU*) that provides readings of the robot's roll and pitch angles with respect to a horizontal plane [32].

Then, a frame was defined for the robot ($X_cY_cZ_c$) whose X_cY_c plane coincides with the plane containing the four contact points of the wheels with the ground. The X_c axis aligns with the longitudinal direction of the robot (forward), the Z_c axis is perpendicular to this plane, and the origin O_c is located at the intersection of the axis of the first joint in the robot's arm with the X_cY_c plane (Figure 2a). From this system, the homogeneous coordinates of the wheel contact point with the ground (${}^cP_1, {}^cP_2, {}^cP_3, {}^cP_4$), along with the coordinates of the end effector of the arm corresponding to an omnidirectional wheel (${}^cP_5$), can be defined using (1), whose variables can be determined by observing Figure 2. The magnitudes of these variables are shown in Table 1. Additionally, all the variables used in the equations are defined in an appendix located at the end of the article.

$$
\begin{aligned}
{}^cP_1 &= \begin{bmatrix} {}^cx_1 \\ {}^cy_1 \\ {}^cz_1 \\ 1 \end{bmatrix} = \begin{bmatrix} x_f + \Delta x_f \\ y_t/2 \\ 0 \\ 1 \end{bmatrix} \\
{}^cP_2 &= \begin{bmatrix} {}^cx_2 \\ {}^cy_2 \\ {}^cz_2 \\ 1 \end{bmatrix} = \begin{bmatrix} x_f + \Delta x_f \\ -y_t/2 \\ 0 \\ 1 \end{bmatrix} \\
{}^cP_3 &= \begin{bmatrix} {}^cx_3 \\ {}^cy_3 \\ {}^cz_3 \\ 1 \end{bmatrix} = \begin{bmatrix} -x_r + \Delta x_r \\ -y_t/2 \\ 0 \\ 1 \end{bmatrix} \\
{}^cP_4 &= \begin{bmatrix} {}^cx_4 \\ {}^cy_4 \\ {}^cz_4 \\ 1 \end{bmatrix} = \begin{bmatrix} -x_r + \Delta x_r \\ y_t/2 \\ 0 \\ 1 \end{bmatrix} \\
{}^cP_5 &= \begin{bmatrix} {}^cx_5 \\ {}^cy_5 \\ {}^cz_5 \\ 1 \end{bmatrix} = \begin{bmatrix} a_1 c\theta_1 \\ a_1 s\theta_1 \\ d_2 - d_{2c} \\ 1 \end{bmatrix}
\end{aligned}
\tag{1}
$$

Additionally, it is important to note that in (1), Δx_f and Δx_r appear, which correspond to variations in the position of the front and rear wheel contact points, respectively (from the ideal position). These variations occur when the wheels are positioned on surfaces that are not parallel to the X_cY_c plane (see Figure 2b). On the other hand, if all the wheels are on the same flat surface, $\Delta x_f = \Delta x_r = 0$. Although this change in the position of the wheel contact points with the ground also induces a variation in the Z_c direction, called Δz, it will be assumed negligible due to its very small magnitude.

On the other hand, an imaginary rectangle was defined on the X_cY_c plane that encompasses the orthogonal projection of all the constituent parts of the robot (Figure 3). This rectangle, whose vertices are ${}^cE_n({}^cx_{En}, {}^cy_{En}, 0)$ with $n = 1...4$, was defined to ensure that no part of the robot collides with the obstacle during the overcoming task. Additionally, the arm was excluded from the definition of the robot's bounding rectangle since, during strategy phases where collisions between the arm and the obstacle could occur, the arm is retracted to prevent such interactions.

https://doi.org/10.1017/S0263574725000542 Published online by Cambridge University Press

Table 1. *Dimensional parameters of the Lázaro robot.*

Parameter	Magnitude (mm)
x_f	209.0
x_r	191.0
x_t	400.0
y_t	398.0
a_1	420.0
d_{2c}	−282.5
R_r	75.0

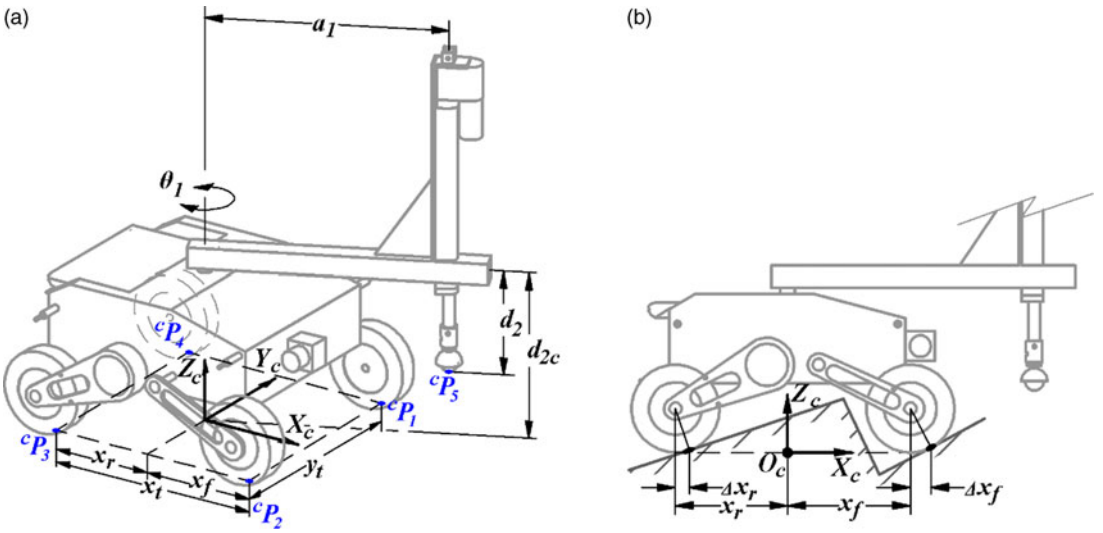


Figure 2. *Lázaro robot showing dimensions and $X_cY_cZ_c$ frame. (a) Axonometric view; (b) Side view.*

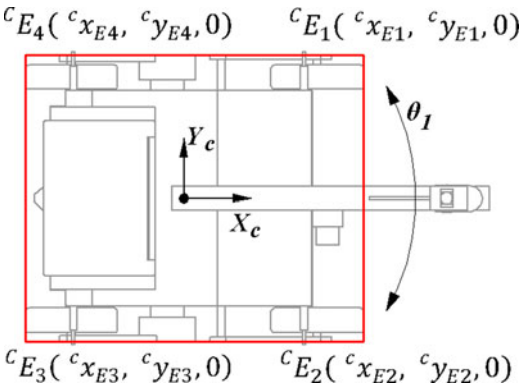


Figure 3. *Top view of the Lázaro robot showing the safety rectangle.*

Finally, to transform the homogeneous coordinates of any point defined in the $X_cY_cZ_c$ frame (either ^cP_n or ^cE_n) to the $X_MY_MZ_M$ frame, Eq. (2) must be used, where ^MT_c is the homogeneous transformation matrix of the $X_cY_cZ_c$ frame with respect to the $X_MY_MZ_M$ frame. It is worth noting that this matrix includes the roll angle (α_c) and pitch angle (ϕ_c) of the robot (continuously obtained using the IMU; see Figure 4), and the coordinates of the point O_c (origin of the $X_cY_cZ_c$ frame) represented in a fixed global $X_MY_MZ_M$ frame as $^MO_c(^Mx_{Oc}, ^My_{Oc}, ^Mz_{Oc})$, which define the position of the robot and must be constantly obtained during the development of the overcoming strategy.

https://doi.org/10.1017/S0263574725000542 Published online by Cambridge University Press

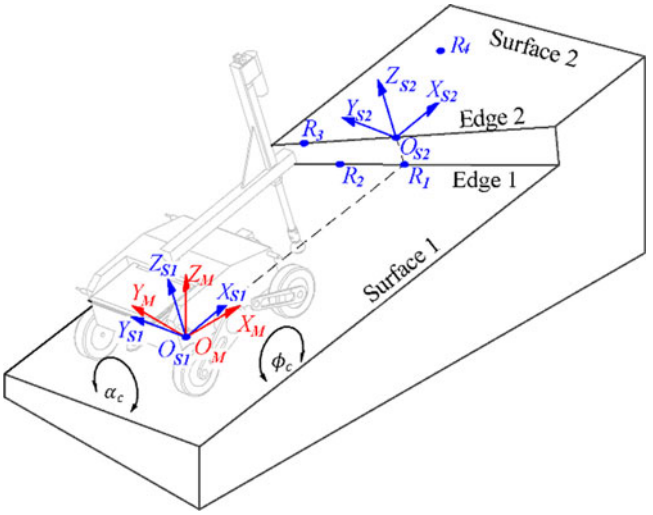


Figure 4. *Geometric parameters used to characterize the obstacle.*

$$ {}^{M}P_n = \begin{bmatrix} {}^{M}x_n \\ {}^{M}y_n \\ {}^{M}z_n \\ 1 \end{bmatrix} = {}^{M}T_c\,{}^{c}P_n = \begin{bmatrix} c\phi_c & s\phi_c s\alpha_c & s\phi_c c\alpha_c & {}^{M}x_{Oc} \\ 0 & c\alpha_c & -s\alpha_c & {}^{M}y_{Oc} \\ -s\phi_c & c\phi_c s\alpha_c & c\phi_c c\alpha_c & {}^{M}z_{Oc} \\ 0 & 0 & 0 & 1 \end{bmatrix} \begin{bmatrix} {}^{c}x_n \\ {}^{c}y_n \\ {}^{c}z_n \\ 1 \end{bmatrix} \tag{2} $$

2.3. Characterization of the obstacle

In accordance with the established premises, an obstacle was defined as two simplified flat surfaces: *Surface 1*, where the robot is located before overcoming the obstacle, and *Surface 2*, where the robot is positioned after overcoming the obstacle (Figure 4). These surfaces are delimited by two considered straight edges: *Edge 1* defines *Surface 1*, and *Edge 2* defines *Surface 2*. The space between the edges defines the obstacle that will not be touched by the robot at any point. Now, based on this, three frames were defined (Figure 4):

a. A fixed frame ($X_{s1}Y_{s1}Z_{s1}$) attached to *Surface 1*, where the $X_{s1}Y_{s1}$ plane is contained within *Surface 1*, the Z_{s1} axis is perpendicular to this surface, and the origin of this frame O_{s1} coincides with the point O_c at an initial time ($t = 0$) when the robot has not initiated the obstacle overcoming process. At that moment, $X_{s1}Y_{s1}Z_{s1}$ coincides with $X_cY_cZ_c$.
b. A fixed global frame ($X_MY_MZ_M$) where X_MY_M is located on a horizontal plane, the X_M axis coincides with the horizontal projection of X_{s1}, Z_M is vertical, and the origin O_M coincides with O_{s1}.
c. A fixed frame ($X_{s2}Y_{s2}Z_{s2}$), attached to *Surface 2*, where the $X_{s2}Y_{s2}$ plane is contained within *Surface 2*, the Z_{s2} axis is perpendicular to this surface, the origin of this frame O_{s2} coincides with the intersection of *Edge 2* with the $X_{s1}Z_{s1}$ plane, and the X_{s2} axis coincides with the intersection of *Surface 2* with the $X_{s1}Z_{s1}$ plane.

To perform a simple characterization of the obstacle, the position coordinates of 5 points are acquired with respect to the $X_{s1}Y_{s1}Z_{s1}$ frame:

a. Point R_1: defined by the intersection of the $X_{s1}Z_{s1}$ plane with *Edge 1* (Figure 4).
b. Point R_2: any point belonging to *Edge 1*, provided that $R_2 \neq R_1$.

https://doi.org/10.1017/S0263574725000542 Published online by Cambridge University Press

c. Point O_{s2}, already defined previously.
d. Point R_3: any point belonging to *Edge 2*, provided that $R_3 \neq O_{s2}$.
e. Point R_4: any point belonging to *Surface 2*, provided that $R_4 \notin$ *Edge 2*.

Finally, the orientation of the $X_{s1}Y_{s1}Z_{s1}$ and $X_{s2}Y_{s2}Z_{s2}$ frames with respect to the fixed $X_MY_MZ_M$ frame must be established using the *Roll* (α) and *Pitch* (ϕ) angles. Therefore, the following angles are defined:

a. α_{s1}, ϕ_{s1}: *roll* and *pitch* angles of the $X_{s1}Y_{s1}Z_{s1}$ frame with respect to the $X_MY_MZ_M$ frame (define the inclination of *Surface 1* with respect to horizontal plane).
b. α_{s2}, ϕ_{s2}: *roll* and *pitch* angles of the $X_{s2}Y_{s2}Z_{s2}$ frame with respect to the $X_MY_MZ_M$ frame (define the inclination of *Surface 2* with respect to horizontal plane).

Mathematical characterization of Surface 1: Knowing that this surface is defined by the angles (α_{s1}, ϕ_{s1}) and that at the beginning of the strategy, the $X_{s1}Y_{s1}Z_{s1}$ frame is superimposed on $X_cY_cZ_c$, it can be stated that $\alpha_{s1} = \alpha_c$ and $\phi_{s1} = \phi_c$ when $t = 0$. Therefore, these angles can be obtained through the robot's IMU. Now, given a point ${}^{s1}P = [{}^{s1}x, {}^{s1}y, {}^{s1}z, 1]^T$ in the $X_{s1}Y_{s1}Z_{s1}$ frame, it can be considered through the coordinate ${}^{s1}z$ that: ${}^{s1}P$ is under *Surface 1* (${}^{s1}z < 0$), ${}^{s1}P$ is contained within *Surface 1* (${}^{s1}z = 0$) or ${}^{s1}P$ is over *Surface 1* (${}^{s1}z > 0$).

On the other hand, if a point ${}^{M}P$ is available in the $X_MY_MZ_M$ frame, its coordinates can be expressed in the $X_{s1}Y_{s1}Z_{s1}$ frame through (3), resulting in ${}^{s1}P$. This then allows determining the relative position of the point with respect to *Surface 1*.

$$ {}^{s1}P = \begin{bmatrix} {}^{s1}x \\ {}^{s1}y \\ {}^{s1}z \\ 1 \end{bmatrix} = {}^{s1}T_M\,{}^{M}P = \begin{bmatrix} c\phi_{s1} & 0 & -s\phi_{s1} & 0 \\ s\phi_{s1}s\alpha_{s1} & c\alpha_{s1} & c\phi_{s1}s\alpha_{s1} & 0 \\ s\phi_{s1}c\alpha_{s1} & -s\alpha_{s1} & c\phi_{s1}c\alpha_{s1} & 0 \\ 0 & 0 & 0 & 1 \end{bmatrix} \begin{bmatrix} {}^{M}x \\ {}^{M}y \\ {}^{M}z \\ 1 \end{bmatrix} \tag{3} $$

Mathematical characterization of Surface 2: Similar to *Surface 1*, this surface will be defined by the $X_{s2}Y_{s2}Z_{s2}$ frame and the angles (α_{s2}, ϕ_{s2}), which are obtained using the coordinates of points O_{s2}, R_3 and R_4 defined with respect to $X_{s1}Y_{s1}Z_{s1}$; these are: ${}^{s1}O_{s2}({}^{s1}x_{O2}, 0, {}^{s1}z_{O2})$, ${}^{s1}R_3({}^{s1}x_{R3}, {}^{s1}y_{R3}, {}^{s1}z_{R3})$ and ${}^{s1}R_4({}^{s1}x_{R4}, {}^{s1}y_{R4}, {}^{s1}z_{R4})$. Using them, the coordinates of the vectors $\overrightarrow{O_{s2}R_3}$ and $\overrightarrow{O_{s2}R_4}$ can be defined. Then, ${}^{s1}\vec{U}_{Z_{s2}}$, which is the unit vector of the Z_{s2} axis with respect to the $X_{s1}Y_{s1}Z_{s1}$ frame, can be found:

$$ {}^{s1}\vec{U}_{Z_{s2}} = \begin{cases} \dfrac{\overrightarrow{O_{s2}R_4} \times \overrightarrow{O_{s2}R_3}}{\left|\overrightarrow{O_{s2}R_4} \times \overrightarrow{O_{s2}R_3}\right|} \forall {}^{s1}y_{R3} > 0 \\ \dfrac{\overrightarrow{O_{s2}R_3} \times \overrightarrow{O_{s2}R_4}}{\left|\overrightarrow{O_{s2}R_3} \times \overrightarrow{O_{s2}R_4}\right|} \forall {}^{s1}y_{R3} < 0 \end{cases} \tag{4} $$

The coordinates of this vector are transformed to a frame parallel to $X_MY_MZ_M$ with the origin at O_{s2} to obtain ${}^{\|M}\vec{U}_{Z_{s2}}$:

$$ {}^{\|M}\vec{U}_{Z_{s2}} = \begin{bmatrix} {}^{\|M}x_{z_{s2}} \\ {}^{\|M}y_{z_{s2}} \\ {}^{\|M}z_{z_{s2}} \end{bmatrix} = \begin{bmatrix} c\phi_{s1} & s\phi_{s1}s\alpha_{s1} & s\phi_{s1}c\alpha_{s1} \\ 0 & c\alpha_{s1} & -s\alpha_{s1} \\ -s\phi_{s1} & c\phi_{s1}s\alpha_{s1} & c\phi_{s1}c\alpha_{s1} \end{bmatrix} {}^{s1}\overrightarrow{U}_{Z_{s2}} \tag{5} $$

Finally, from (5), it is possible to obtain ϕ_{s2} and α_{s2} through (6) and (7):

$$ \phi_{s2} = \tan^{-1}\left(\frac{{}^{\|M}x_{z_{s2}}}{{}^{\|M}z_{z_{s2}}}\right) \tag{6} $$

$$ \alpha_{s2} = \tan^{-1}\left(\frac{-{}^{\|M}y_{z_{s2}}}{\sqrt{1 - {}^{\|M}y_{z_{s2}}}}\right) \tag{7} $$

https://doi.org/10.1017/S0263574725000542 Published online by Cambridge University Press

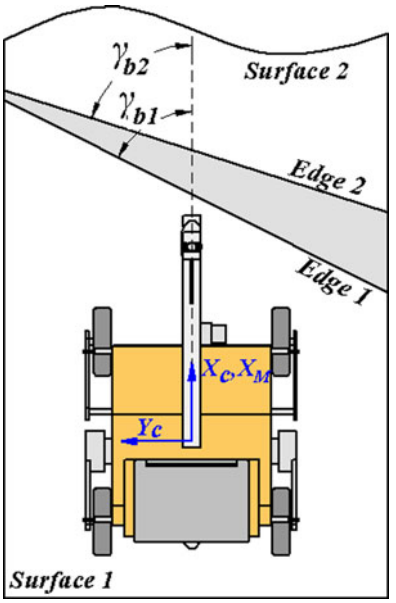


Figure 5. *Top view of the Lázaro robot and obstacle highlighting the angles* $\boldsymbol{\gamma}_{b1}$ *and* $\boldsymbol{\gamma}_{b2}$.

Now, it is important to determine whether a given point ${}^{M}P$ in the $X_M Y_M Z_M$ frame is contained in *Surface 2*; for this, its coordinates expressed in the $X_{s2} Y_{s2} Z_{s2}$ frame must be found through (8), resulting in ${}^{s2}P$:

$$
\begin{aligned}
{}^{s2}P &= \begin{bmatrix} {}^{s2}x \\ {}^{s2}y \\ {}^{s2}z \\ 1 \end{bmatrix} = {}^{s2}T_M \, {}^{M}P \\
&= \begin{bmatrix} c\phi_{s2} & 0 & -s\phi_{s2} & -\left({}^{M}x_{O2} c\phi_{s2} - {}^{M}z_{O2} s\phi_{s2}\right) \\ s\phi_{s2} s\alpha_{s2} & c\alpha_{s2} & c\phi_{s2} s\alpha_{s2} & -\left({}^{M}x_{O2} s\phi_{s2} s\alpha_{s2} + {}^{M}y_{O2} c\alpha_{s2} + {}^{M}z_{O2} c\phi_{s2} s\alpha_{s2}\right) \\ s\phi_{s2} c\alpha_{s2} & -s\alpha_{s2} & c\phi_{s2} c\alpha_{s2} & -\left({}^{M}x_{O2} s\phi_{s2} c\alpha_{s2} - {}^{M}y_{O2} s\alpha_{s2} + {}^{M}z_{O2} c\phi_{s2} c\alpha_{s2}\right) \\ 0 & 0 & 0 & 1 \end{bmatrix} \begin{bmatrix} {}^{M}x \\ {}^{M}y \\ {}^{M}z \\ 1 \end{bmatrix}
\end{aligned}
\tag{8}
$$

Then, it can be stated that: ${}^{s2}P$ is under *Surface 2* (${}^{s2}z < 0$), ${}^{s2}P$ is contained within *Surface 2* (${}^{s2}z = 0$) or ${}^{s2}P$ is over *Surface 2* (${}^{s2}z > 0$).

Mathematical characterization of Edge 1: As previously mentioned, the edges were simplified as straight lines. In the case of *Edge 1*, it is defined by points R_1 and R_2, whose coordinates in the $X_{s1} Y_{s1} Z_{s1}$ frame are given by: ${}^{s1}R_1({}^{s1}x_{R1}, 0, 0, 1)$ and ${}^{s1}R_2({}^{s1}x_{R2}, {}^{s1}y_{R2}, 0, 1)$. These coordinates can be transformed into the $X_M Y_M Z_M$ frame to obtain ${}^{M}R_1({}^{M}x_{R1}, {}^{M}y_{R1}, {}^{M}z_{R1}, 1)$ and ${}^{M}R_2({}^{M}x_{R2}, {}^{M}y_{R2}, {}^{M}z_{R2}, 1)$. From this, the projection of *Edge 1* onto the $X_M Y_M$ plane can be defined as a line with slope m, ordinate b (defines the point of intersection between the line and the Y_M axis) and the angle γ_{b1} (9), which gives the inclination of the line with respect to the X_M axis (Figure 5):

$$
\begin{cases} \gamma_{b1} = \tan^{-1}\left(\frac{{}^{M}y_{R2} - {}^{M}y_{R1}}{{}^{M}x_{R2} - {}^{M}x_{R1}}\right) & \forall {}^{M}x_{R1} \neq {}^{M}x_{R2} \\ \gamma_{b1} = 90^{\circ} & \forall {}^{M}x_{R1} = {}^{M}x_{R2} \end{cases}
\tag{9}
$$

https://doi.org/10.1017/S0263574725000542 Published online by Cambridge University Press

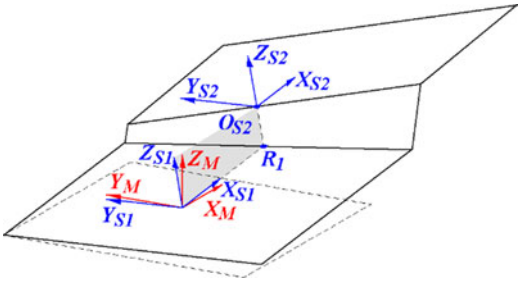


Figure 6. *Axonometric perspective of the obstacle.*

Finally, to determine whether the projection of a point ${}^{M}P({}^{M}x, {}^{M}y, {}^{M}z)$ is located before, on, or after *Edge 1*, its coordinates should be evaluated using (10):

$$\left.\begin{array}{l} {}^{M}y - m{}^{M}x < b \wedge \gamma_{b1} > 90^{\circ} \\ {}^{M}x < {}^{M}x_{R1} \wedge \gamma_{b1} = 90^{\circ} \\ {}^{M}y - m{}^{M}x > b \wedge \gamma_{b1} < 90^{\circ} \end{array}\right\} {}^{M}P \text{ is before edge 1}$$

$$\left.\begin{array}{l} {}^{M}y - m{}^{M}x = b \wedge \gamma_{b1} \neq 90^{\circ} \\ {}^{M}x = {}^{M}x_{R1} \wedge \gamma_{b1} = 90^{\circ} \end{array}\right\} {}^{M}P \in \text{ edge 1}$$

$$\left.\begin{array}{l} {}^{M}y - m{}^{M}x < b \wedge \gamma_{b1} < 90^{\circ} \\ {}^{M}x > {}^{M}x_{R1} \wedge \gamma_{b1} = 90^{\circ} \\ {}^{M}y - m{}^{M}x > b \wedge \gamma_{b1} > 90^{\circ} \end{array}\right\} {}^{M}P \text{ is after edge 1} \tag{10}$$

Mathematical characterization of Edge 2: Similar to Edge 1, this edge will be defined by the points O_{s2} and R_3, whose coordinates in the $X_{s1}Y_{s1}Z_{s1}$ frame are given by: ${}^{s1}O_{s2}({}^{s1}x_{O2}, 0, {}^{s1}z_{O2}, 1)$ and ${}^{s1}R_3({}^{s1}x_{R3}, {}^{s1}y_{R3}, {}^{s1}z_{R3}, 1)$. These coordinates can be transformed into the $X_MY_MZ_M$ frame to obtain ${}^{M}O_{s2}({}^{M}x_{O2}, {}^{M}y_{O2}, {}^{M}z_{O2}, 1)$ and ${}^{M}R_3({}^{M}x_{R3}, {}^{M}y_{R3}, {}^{M}z_{R3}, 1)$. From this, the projection of Edge 2 onto the X_MY_M plane can be defined as a line given by its slope m, the ordinate b (defines the point of intersection between the line and the Y_M axis) and the angle γ_{b2} (11), which gives the inclination of this line with respect to the X_M axis (Figure 5):

$$\begin{cases} \gamma_{b2} = \tan^{-1}\left(\dfrac{{}^{M}y_{R3} - {}^{M}y_{O2}}{{}^{M}x_{R3} - {}^{M}x_{O2}}\right) \forall {}^{M}x_{O2} \neq {}^{M}x_{R3} \\ \gamma_{b2} = 90^{\circ} \qquad\qquad {}^{M}x_{O2} = {}^{M}x_{R3} \end{cases} \tag{11}$$

Finally, to determine if the projection of a point ${}^{M}P({}^{M}x, {}^{M}y, {}^{M}z)$ is located before or after *Edge 2*, its coordinates can be evaluated using (10) considering γ_{b2} instead of γ_{b1}.

Characterization of the obstacle shape: a cut was made to the obstacle using the plane $X_{s1}Z_{s1}$ (shaded plane in Figure 6) and then studying the coordinates of the points ${}^{s1}R_1({}^{s1}x_{R1}, 0, 0)$ and ${}^{s1}O_{s2}({}^{s1}x_{O2}, 0, {}^{s1}z_{O2})$. The shape of the obstacle will be determined by (12) and Figure 7:

$$\begin{array}{l} {}^{s1}z_{O2} > 0 \bigwedge \begin{cases} {}^{s1}x_{O2} - {}^{s1}x_{R1} > 0 \; \textit{Ascending ramp} \\ {}^{s1}x_{O2} - {}^{s1}x_{R1} = 0 \; \textit{Ascending step} \\ {}^{s1}x_{O2} - {}^{s1}x_{R1} < 0 \; \textit{Ascending inverted ramp} \end{cases} \\ {}^{s1}z_{O2} = 0 \bigwedge \{ {}^{s1}x_{O2} - {}^{s1}x_{R1} = 0 \; \textit{Ditch} \\ {}^{s1}z_{O2} < 0 \bigwedge \begin{cases} {}^{s1}x_{O2} - {}^{s1}x_{R1} > 0 \; \textit{Descending ramp} \\ {}^{s1}x_{O2} - {}^{s1}x_{R1} = 0 \; \textit{Descending step} \\ {}^{s1}x_{O2} - {}^{s1}x_{R1} < 0 \; \textit{Descending inverted ramp} \end{cases} \end{array} \tag{12}$$

https://doi.org/10.1017/S0263574725000542 Published online by Cambridge University Press

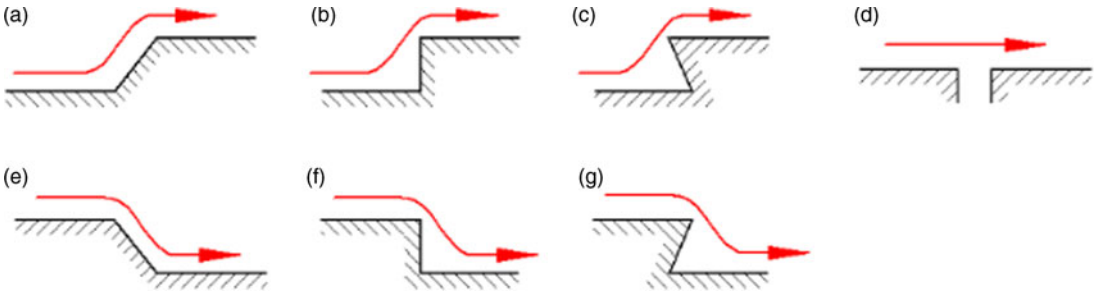


Figure 7. *Forms of the obstacle. Ascending: (a) Ramp, (b) Step, (c) Inverted ramp. At the same level: (d) Trench. Descending: (e) Ramp, (f) Step, (g) Inverted ramp.*

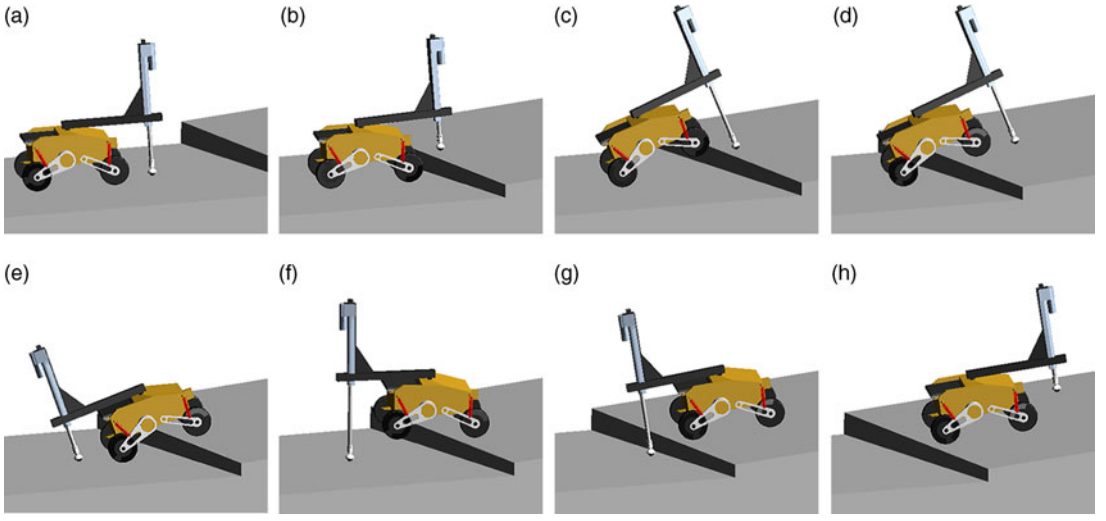


Figure 8. *Stages for overcoming obstacles by first lifting the front wheels.*

3. Definition of the strategy to overcome obstacles

In this strategy, overcoming the obstacle is achieved when the robot lifts a pair of wheels at a time to position them over the obstacle and then lifts the remaining pair. The first pair of wheels that successfully clears the obstacle will hereinafter be referred to as the *near wheels*, while the last pair of wheels that clears the obstacle will be referred to as the *far wheels*. Subsequently, the determination of which pair of wheels will initiate the overcoming (*near wheels*) will depend on the orientation of the robot with respect to the obstacle: if $45° \leq \gamma_{b1} \leq 135°$, the front wheels will be lifted first to achieve overcoming; otherwise, the right wheels ($0° < \gamma_{b1} < 45°$) or the left wheels ($135° < \gamma_{b1} < 180°$) will be lifted first. In general, the strategy is completed with the execution of 8 stages for any type of obstacle, regardless of which wheels will be the *near wheels*: front (Figure 8) or a pair of lateral wheels (Figure 9). These stages are described in a general manner below:

a. ***Positioning in front of the obstacle:*** occurs when the presence of an obstacle is detected. The characterization of this is carried out, and the arm is prepared for the operation, placing it in the front position ($\theta_1 = 0°$) and fully retracting the second link (Figure 8a and Figure 9a).
b. ***Deployment of the arm over the obstacle:*** the robot moves towards the obstacle and rotates the arm until its end effector is positioned beyond the obstacle (beyond *Edge 2*) and in a suitable position. Then, the second link of the arm is deployed until its end effector touches *Surface 2* (Figures 8b and 9b).

https://doi.org/10.1017/S0263574725000542 Published online by Cambridge University Press

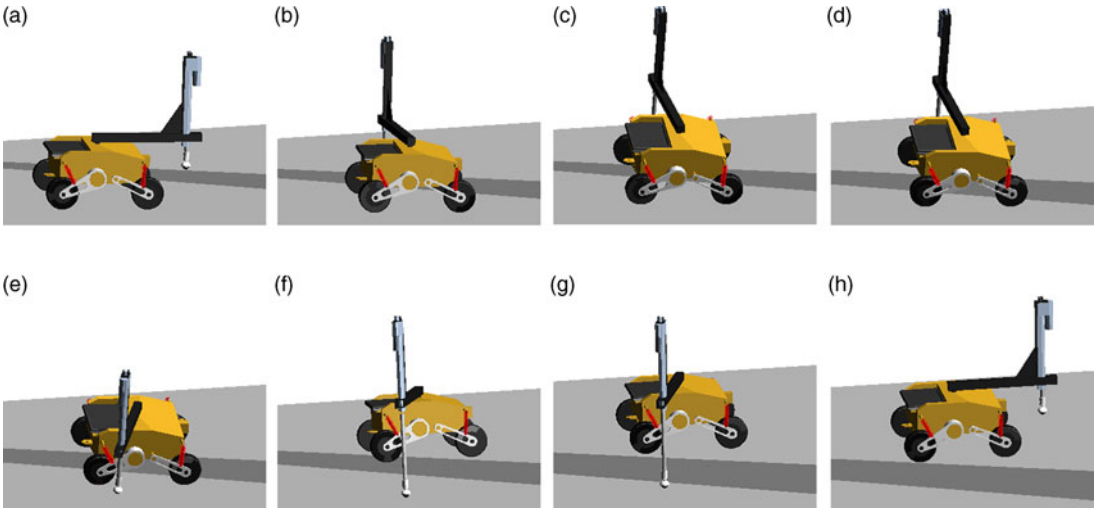


Figure 9. *Stages for overcoming obstacles by first lifting the lateral wheels.*

c. ***Initial elevation of the robot with the support of the arm:*** the second link of the arm continues to deploy until the two *near wheels* lose contact with the ground and rise to overcome the height of the obstacle (Figures 8c and 9c).

d. ***Advancement of the robot using the distant wheels:*** With the robot supported by the two *far wheels* and the end effector of the arm, the traction of the robot is activated, causing it to advance pulled by its *far wheels* until the *near wheels* surpass the obstacle, that is, they have passed over *Edge 2* (Figures 8d and 9d).

e. ***Repositioning of the arm to lift the distant wheels:*** The arm retracts completely, leaving the robot supported on its *near wheels* that touch *Surface 2*. Then, the first link of the arm rotates to position itself properly, followed by the deployment of the second link until its end effector touches *Surface 1* (Figures 8e and 9e).

f. ***Final elevation of the robot with arm support:*** The second link of the arm continues to deploy until the two *far wheels* are raised to surpass the height of the obstacle (Figures 8f and 9f).

g. ***Robot advance using the near wheels:*** With the robot supported by the two *near wheels* and the arm's end effector, the robot's traction is activated to move forward driven by its *near wheels* until the *far wheels* surpass the obstacle, that is, have crossed over *Edge 2* (Figures 8g and 9g).

h. ***Landing:*** The second link of the arm retracts completely; during this process, the *far wheels* touch *Surface 2* (after the obstacle), leaving the robot supported on its 4 wheels. Subsequently, the first joint rotates until the arm reaches its original position (Figures 8h and 9h).

Each stage is described in detail along with the sequential movements required. A program was developed to replicate these stages, accounting for time variations (Δt) and simulating displacements and rotations using equations and homogeneous transformations to ensure geometric fulfillment of the defined conditions. At each time increment, the following variables are computed: roll (α_c) and pitch (ϕ_c) angles, arm joint variables (θ_1, d_2), and the robot's position (${}^M x_{Oc}, {}^M y_{Oc}, {}^M z_{Oc}$) relative to the $X_M Y_M Z_M$ frame. The final values of these variables upon completing each stage are stored as *setpoints* for the robot's actuators to achieve, ensuring full execution of the corresponding stage.

Stage a. Positioning in front of the obstacle

At the beginning of this stage, the obstacle is characterized, and the initial position of the robot $({}^M x_{Oc}, {}^M y_{Oc}, {}^M z_{Oc}) = (0, 0, 0)$, the joint variables of the arm (θ_1, d_2), and the angles α_c and ϕ_c (using the

https://doi.org/10.1017/S0263574725000542 Published online by Cambridge University Press

robot's IMU) are defined for the initial instant $t = 0$ s. From this, ***Movement 1*** is generated, where the second link of the arm is fully retracted at a reference speed V_{d2}, and the arm is positioned forward by rotating it at a speed $\omega_{\theta 1}$, resulting in $\theta_1 = 0°$.

Stage b. Arm deployment over the slope

To achieve the goal of this stage, the robot must perform three consecutive movements:

Movement 2: The robot advances at a reference speed V_c until one of the two points located in front of the safety rectangle (E_1 or E_2, see Figure 3) is over *Edge 1*. This advance is defined for each time instant (Δt) as $\Delta x = V_c \Delta t$, which is added to the ${}^{s1}x_{Oc}$ coordinate of the robot in the $X_{s1}Y_{s1}Z_{s1}$ frame. Then, using (13), the positions of ${}^{s1}E_1$ and ${}^{s1}E_2$ in the $X_{s1}Y_{s1}Z_{s1}$ frame can be obtained. Finally, these points are transformed into the $X_M Y_M Z_M$ frame (updating the robot's position ${}^{M}O_c$) and evaluated until one of them reaches *Edge 1* using (10):

$$ {}^{s1}E_n = \begin{bmatrix} {}^{s1}x_{Oc} \\ 0 \\ 0 \end{bmatrix} + {}^{c}E_n \tag{13} $$

with ${}^{c}E_n$ defined in Figure 3.

Movement 3: The robot rotates the first link of its arm to the target position, $\theta_{1\,sp}$, ensuring the end-effector moves beyond *Edge 2*. A fuzzy system was designed for this, using β_1, β_2, and γ_{b1} as input variables (antecedents), where $\beta_1$and β_2 represent the maximum slope director angles of *Surfaces 1* and *2*, derived from their roll (α_{si}) and pitch (ϕ_{si}), as defined by (14), with $i = \{1, 2\}$ (Figure 10). Seven fuzzy sets were defined for each input within the ranges: $\beta_1 \in [-180°,180°]$, $\beta_2 \in [-180°,180°]$, and $\gamma_{b1} \in [0,180°]$. For the output ($\theta_{1\,sp}$), 17 fuzzy sets were distributed across $[-180°,180°]$. A total of 343 fuzzy rules were established based on observations of a static robotic model tested on inclined obstacles, aimed at improving stability by adjusting the arm's position. The relationship between two input variables (with the third held constant) and the output $\theta_{1\,sp}$ is visualized through the 3D surfaces in Figure 11, illustrating the fuzzy system's behavior in specific scenarios.

$$ \beta_i = \tan^{-1}\left(\frac{-\sin\alpha_{si}\cos\phi_{si}}{\sin\phi_{si}}\right) \tag{14} $$

Movement 4: The second link of the arm is deployed until the end effector touches *Surface 2*. At this instant, the second link has a length d_2 obtained from (15) knowing the position of the robot (${}^{M}x_{Oc}$, ${}^{M}y_{Oc}$, ${}^{M}z_{Oc}$) relative to the $X_M Y_M Z_M$ frame:

$$ d_2 = d_{2c} - \frac{n_z\left(a_1 c\theta_1 c\phi_c + a_1 s\theta_1 s\phi_c s\alpha_c + {}^{M}x_{Oc}\right) + o_z\left(a_1 s\theta_1 c\alpha_c + {}^{M}y_{Oc}\right) + a_z\left(-a_1 c\theta_1 s\phi_c + a_1 s\theta_1 c\phi_c s\alpha_c + {}^{M}z_{Oc}\right) + p_z}{n_z s\phi_c c\alpha_c - o_z s\alpha_c + a_z c\phi_c c\alpha_c} \tag{15} $$

with:

$$ \begin{aligned} n_z &= s\phi_{s2} c\alpha_{s2} \\ o_z &= -s\alpha_{s2} \\ a_z &= c\phi_{s2} c\alpha_{s2} \\ p_z &= -\left({}^{M}x_{O2} s\phi_{s2} c\alpha_{s2} - {}^{M}y_{O2} s\alpha_{s2} + {}^{M}z_{O2} c\phi_{s2} c\alpha_{s2}\right) \end{aligned} \tag{16} $$

Stage c. Initial elevation of the robot with arm support

Movement 5: The second arm link continues deploying against *Surface 2* until the *near wheels* (front or side, depending on γ_{b1}) clear the obstacle. Simultaneously, the robot rotates about an instantaneous

https://doi.org/10.1017/S0263574725000542 Published online by Cambridge University Press

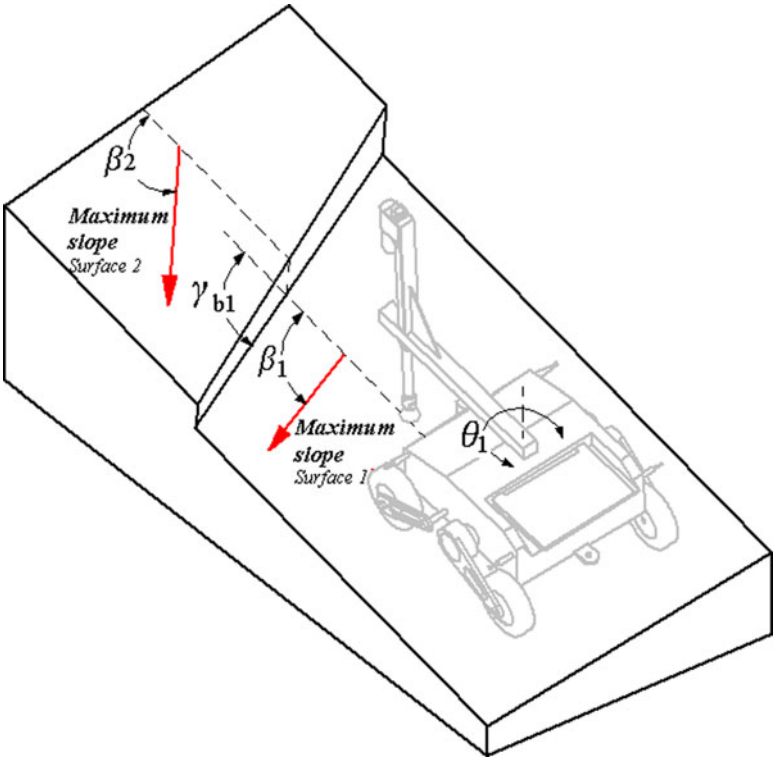


Figure 10. *Parameters used in the fuzzy inference system: antecedents (β_1, β_2, γ_{b1}) and consequent.*

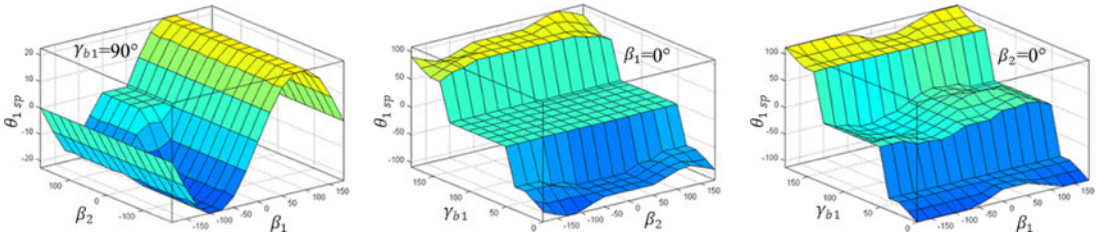


Figure 11. *Surfaces generated for the consequent $\boldsymbol{\theta}_{\mathbf{1}\,sp}$ using the fuzzy inference system.*

axis defined by the *far wheel* contact points, causing changes in ϕ_c (frontal *near wheels*) or α_c (lateral *near wheels*). Initially, $\phi_c = \phi_{s1}$ and $\alpha_c = \alpha_{s1}$. As the movement progresses, variations in ϕ_c or α_c at each Δt allow estimation of a *far wheel n* contact point position, ${}^{s1}P_n = [{}^{s1}x_n, {}^{s1}y_n, {}^{s1}z_n, 1]^T$, where changes depend solely on $\Delta x_r = R_r \sin(\phi_c - \phi_{s1})$. This allows calculation of the (imaginary) contact points of the lifted *near wheels*, ${}^{s1}P_m = [{}^{s1}x_m, {}^{s1}y_m, {}^{s1}z_m, 1]^T$ and ${}^{s1}P_p = [{}^{s1}x_p, {}^{s1}y_p, {}^{s1}z_p, 1]^T$.

The *near wheels* must be lifted until their imaginary contact point heights, ${}^{s1}z_m$ and ${}^{s1}z_p$, surpass the obstacle heights on each robot side, ${}^{s1}z_{1b2}$ and ${}^{s1}z_{2b2}$ (Figure 12), plus a safety margin; this applies to front wheel lifting. For lateral wheels, only the height of the lifted side's obstacle is considered. The obstacle heights, ${}^{s1}z_{1b2}$ and ${}^{s1}z_{2b2}$, are determined using a linear equation representing the projected Edge 2 in the $Y_{s1}Z_{s1}$ plane, substituting the ordinates, ${}^{c}y_{E1}$ and ${}^{c}y_{E2}$, from the safety rectangle (Figure 3).

Stage d. Robot advance using the far wheels

Movement 6: Now, the robot must advance supported by the *far wheels* and the arm's end effector until the *near wheels* (lifted wheels) surpass *Edge 2*, exceeding it by a safety distance d_s. It is expected that, during the advance, the robot maintains the elevation of the lifted wheels achieved in the previous stage

https://doi.org/10.1017/S0263574725000542 Published online by Cambridge University Press

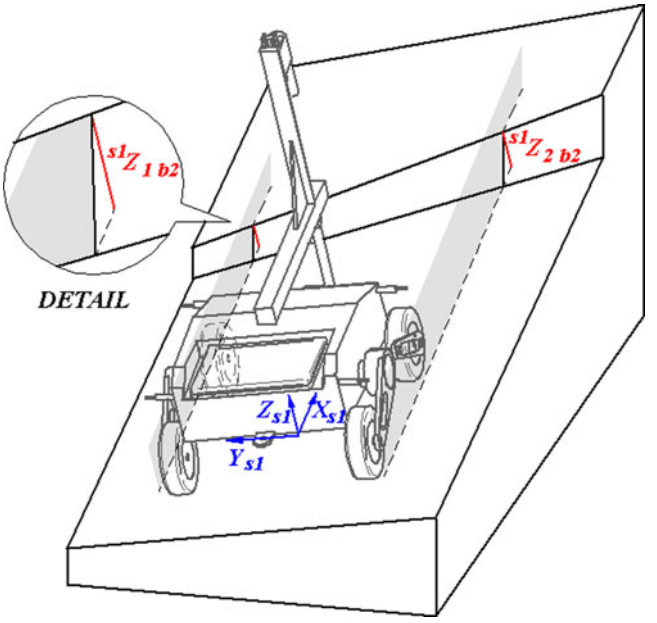


Figure 12. *Heights of the obstacle ($^{s1}z_{1b2}$ and $^{s1}z_{2b2}$) on each side of the robot.*

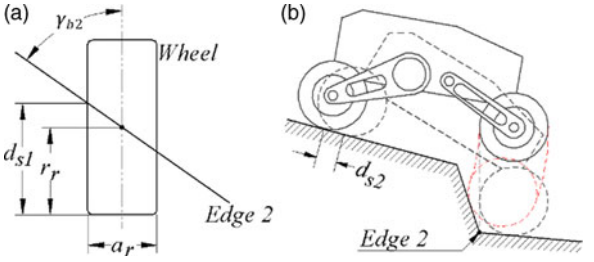


Figure 13. *Factors to determine the safety distance d_s.*

(height above $^{s1}z_{1b2}$ and/or $^{s1}z_{2b2}$). To achieve this, it must keep the angles α_c and ϕ_c constant, which can be achieved by continuously changing the extension of the arm' second link according to (15).

So, let n be a *far wheel* with coordinates of the contact point $^{M}P_n = [^{M}x_n, ^{M}y_n, ^{M}z_n, 1]^T$, its position will be modified as the robot advances with a speed V_c at time intervals Δt. For each moment, the position of the (imaginary) contact points on the *near wheels* can be obtained. These points are used to evaluate whether these wheels have surpassed *Edge 2* according to (10) (considering γ_{b2} instead of γ_{b1}), plus a safety distance d_s, which varies according to the type of obstacle. If the robot is ascending over the obstacle or crossing ditches, $d_s \approx 0$, but when descending from obstacles, d_s must be defined to ensure that, during the following phases, the wheels do not collide with the obstacle. In the case of descent with front wheels, $d_s = d_{s1} + d_{s2}$, where d_{s1} is the distance that ensures that the entire wheel surpasses edge 2 (not just the contact point, see Figure 13a). This distance is defined by (17) and depends on the radius of the wheel r_r and its width a_r.

$$\begin{cases} d_{s1} = \frac{1}{\cos\phi_{s1}} \left(R_r + \frac{a_r}{2|\tan\gamma_{b2}|} \right) & \gamma_{b2} \neq 90^\circ \\ d_{s1} = \frac{R_r}{\cos\phi_{s1}} & \gamma_{b2} = 90^\circ \end{cases} \tag{17}$$

On the other hand, d_{s2} is a distance that compensates for the inward turn that occurs when the wheel (which has already surpassed *Edge 2*) descends from the obstacle (Figure 13b). In the case of Lázaro,

https://doi.org/10.1017/S0263574725000542 Published online by Cambridge University Press

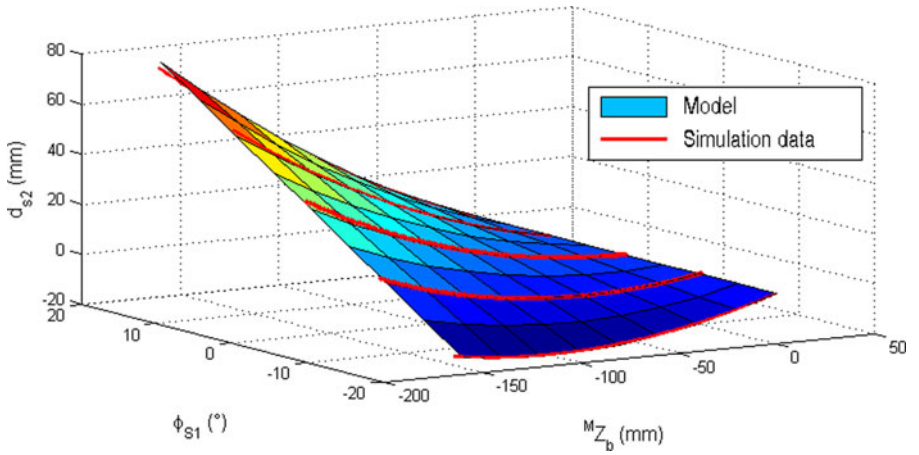


Figure 14. *Development of an empirical model for d_{s2} using data from MSC ADAMS.*

d_{s2} was calculated based on data obtained in multiple simulations using the MSC ADAMS software (Figure 14), and it depends on ${}^{M}z_b$, which is the height of the obstacle on the side of the last wheel that surpasses *Edge 2*. Finally, when evaluating the descent with lateral wheels, $d_s = d_{s1} + d_{s2}/|\tan\gamma_{b2}|$.

Stage e. Repositioning of the arm to lift the far wheels

It consists of four consecutive movements, which are:

Movement 7: involves retracting the second arm link until one or both *near wheels* contact *Surface 2* (behind the obstacle). Concurrently, the robot rotates about an instantaneous axis defined by *the far wheel* contact points, altering ϕ_c (frontal *near wheels*) or α_c (lateral *near wheels*). Considering a *far wheel n*, with initial contact point ${}^{M}P_n = [{}^{M}x_n, {}^{M}y_n, {}^{M}z_n, 1]^T$ (known from the previous stage), its position at each Δt is determined using $\Delta\phi_c$ or $\Delta\alpha_c$ (position changes are solely due to Δx_r). This allows calculation of the robot's position ${}^{M}O_c$, and the *near wheel* contact points, ${}^{M}P_{c1}$ and ${}^{M}P_{c2}$. Note that these *near wheel* contact points are not real until contact with *Surface 2* occurs. However, they are calculated, incorporating $\Delta x_f = R_r \sin(\phi_c - \phi_{s2})$ (Figure 2b), to determine the precise contact position. The movement ceases when a near wheel touches *Surface 2,* verified by evaluating ${}^{M}P_{c1}$ and ${}^{M}P_{c2}$ using the Section 2.3 procedure. The second link extension, d_2, is obtained using (15).

Now, if *Surface 1* and *Surface 2* have differing inclinations, the *near wheels* won't contact *Surface 2* simultaneously. One wheel might touch, leaving the other suspended, potentially requiring a further robot body rotation until both near wheels make contact. This rotation depends on the robot's center of gravity (COG) position relative to the support polygon formed by the wheels contacting the ground. If the COG's horizontal projection lies within the triangle formed by the *far wheel* contact point projections and the *first near wheel* touching the ground, no rotation occurs (Figure 15a). Otherwise (Figure 15b), rotation occurs, positioning the COG within a new triangle formed by the *near wheel* contact points and a *far wheel* (Figure 15c). Let ${}^{H}P_{cn} = [{}^{M}x_{cn}, {}^{M}y_{cn}]^T$, ${}^{H}P_m = [{}^{M}x_m, {}^{M}y_m]^T$, ${}^{H}P_n = [{}^{M}x_n, {}^{M}y_n]^T$, ${}^{H}P_{cs} = [{}^{M}x_{cs}, {}^{M}y_{cs}]^T$ and ${}^{H}P_{COG} = [{}^{M}x_{cog}, {}^{M}y_{cog}]^T$ represent the horizontal plane projections of the *near wheel* c_n (first to contact *Surface 2*), *far wheels m* and *n* (counterclockwise), *near wheel* c_s (contacting after rotation), and the COG respectively. No rotation occurs if the following conditions are met:

$$\overrightarrow{P_nP_m} \times \overrightarrow{P_{cog}P_m} \geq 0 \bigwedge \overrightarrow{P_{cn}P_n} \times \overrightarrow{P_{cog}P_n} \geq 0 \bigwedge \overrightarrow{P_mP_{cn}} \times \overrightarrow{P_{cog}P_n} \geq 0 \tag{18}$$

Otherwise, there will be rotation if:

$$\overrightarrow{P_{cn}P_m} \times \overrightarrow{P_{cog}P_m} \geq 0 \bigwedge \overrightarrow{P_{cs}P_{cn}} \times \overrightarrow{P_{cog}P_{cn}} \geq 0 \bigwedge \overrightarrow{P_mP_{cs}} \times \overrightarrow{P_{cog}P_{cs}} \geq 0 \tag{19}$$

https://doi.org/10.1017/S0263574725000542 Published online by Cambridge University Press

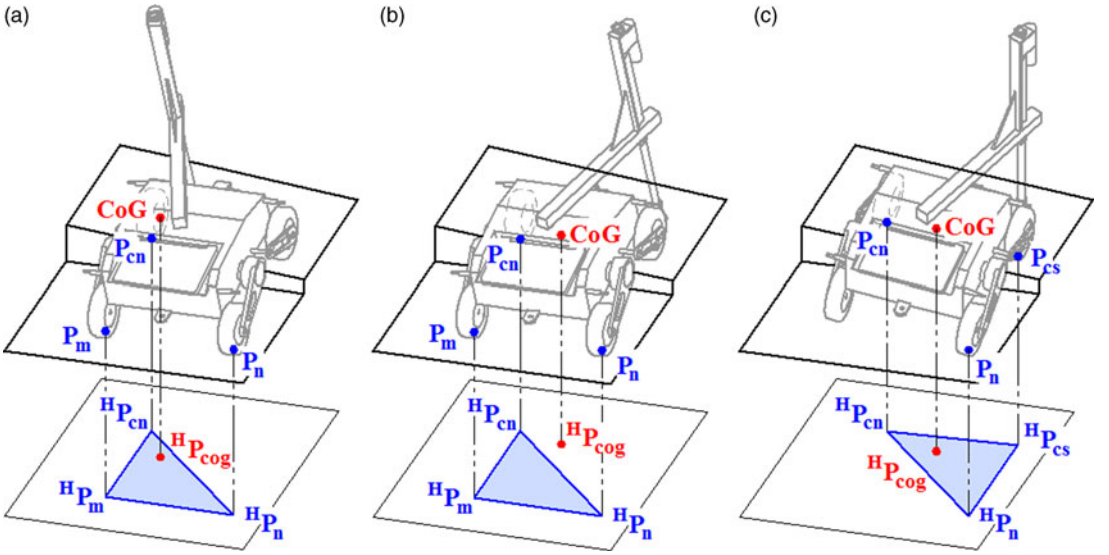


Figure 15. *Rotation process: (a) No rotation exists; (b) Imminent rotation; (c) Robot after rotation.*

On the other hand, when there is rotation, it occurs around an imaginary axis formed by the *near wheel* that has already touched *Surface 2* and the diagonally opposite *far wheel* to it. In practice, this translates into a change in ϕ_c that will continue to vary at intervals of Δt, plus a change in α_c obtained through (20), where the subscripts g_m and g_n correspond to the two wheels that are part of the imaginary pivot axis.

$$\alpha_c = \tan^{-1}\left[\frac{\left({}^{M}z_{gm} - {}^{M}z_{gn}\right) + \sin\phi_c\left({}^{c}z_{gm} - {}^{c}z_{gn}\right)}{\cos\phi_c\left({}^{M}y_{gm} - {}^{M}y_{gn}\right)}\right] \tag{20}$$

This rotation ends when the suspended *near wheel* c_s touches *Surface 2*, so this condition must be continuously evaluated using the procedure described in Section 2.3 with ${}^{M}P_{cs}$. When this rotation is completed, $\alpha_c = \alpha_{s2}$ (*near wheels* are front) or $\phi_c = \phi_{s2}$ (*near wheels* are lateral).

Movement 8: After the end effector of the arm stops touching *Surface 2*, this movement continues with the complete retraction of the second link, which occurs to prevent subsequent collisions when the arm changes position. In this movement, the other geometric and positional parameters of the robot remain constant.

Now, it is important to recall that when *Surfaces 1* and *2* have different inclinations, the phenomenon of involuntary rotation described in *Movement 7* may occur. If it did not occur during that movement, it could occur during the subsequent ones (8, 9, or 10). Therefore, at the end of each movement, the rotation analysis should be performed to assess a possible rotation in the body of the robot due to the position of the COG.

Movement 9: The robot rotates its first arm link to a target position, $\theta_{1\,sp}$, positioning the end effector before *Edge 1*. Another fuzzy logic-based system determines $\theta_{1\,sp}$, prioritizing robot stability. The input variables (antecedents) are β_1, β_2 (14), and γ_{b1}, each using the seven fuzzy sets defined in *Movement 3*. The output (consequent), $\theta_{1\,sp}$, uses seventeen fuzzy sets distributed across 0–360°, mathematically transformed to −180° to 180°. Similar to *Movement 3*, 343 fuzzy rules determine $\theta_{1\,sp}$, visualized as 3D surfaces in Figure 16 (showing examples with two variable antecedents and one constant).

Movement 10: The arm's second link is extended with a speed V_{d2} until the end effector touches *Surface 1*. At that moment, the second arm link has a length d_2 determined by:

https://doi.org/10.1017/S0263574725000542 Published online by Cambridge University Press

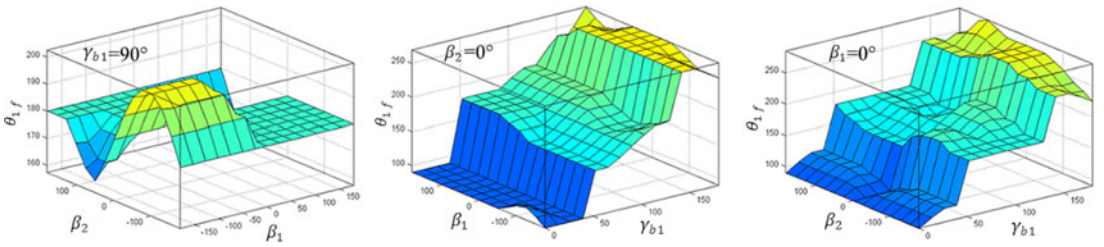


Figure 16. *Surfaces generated for* $\boldsymbol{\theta}_{\mathbf{1}\,sp}$ *using the fuzzy inference system.*

$$d_2 = d_{2c} - \frac{n_z\left(a_1 c\theta_1 c\phi_c + a_1 s\theta_1 s\phi_c s\alpha_c + {}^M x_{Oc}\right) + o_z\left(a_1 s\theta_1 c\alpha_c + {}^M y_{Oc}\right) + a_z\left(-a_1 c\theta_1 s\phi_c + a_1 s\theta_1 c\phi_c s\alpha_c + {}^M z_{Oc}\right)}{n_z s\phi_c c\alpha_c - o_z s\alpha_c + a_z c\phi_c c\alpha_c} \tag{21}$$

with

$$\begin{cases} n_z = s\phi_{s1} c\alpha_{s1} \\ o_z = -s\alpha_{s1} \\ a_z = c\phi_{s1} c\alpha_{s1} \end{cases} \tag{22}$$

Stage f. Final elevation of the robot with the support of the arm

Movement 11: With the end effector contacting *Surface 1*, continued deployment of the second arm link lifts the *far wheels*, clearing the obstacle. This causes robot rotation about an instantaneous axis defined by *the near wheel* contact points, altering ϕ_c (frontal *near wheels*) or α_c (lateral *near wheels*). Considering a *near wheel* contact point, n, with known initial position ${}^M P_n$ in the $X_M Y_M Z_M$ frame, its position is updated at each instant based on ϕ_c or α_c variations (changes due solely to Δx_f). This allows determining the robot's position, ${}^M O_c$, and the positions of the lifting *far wheels*, ${}^{s1}P_{l1} = [{}^{s1}x_{l1}, {}^{s1}y_{l1}, {}^{s1}z_{l1}, 1]^T$ and ${}^{s1}P_{l2} = [{}^{s1}x_{l2}, {}^{s1}y_{l2}, {}^{s1}z_{l2}, 1]^T$. The far wheels are raised until their contact point heights, ${}^{s1}z_{l1}$ and ${}^{s1}z_{l2}$ (imaginary as there's no contact), exceed the obstacle heights on each robot side (${}^{s1}z_{1b1}$ and ${}^{s1}z_{2b2}$; Figure 12) for *frontal wheels*, or the obstacle height on the lifted side for lateral wheels, plus a safety distance, d_s. During this lift, the second arm link extends by d_2, obtained using (21).

Stage g. Advancement of the robot using the near wheels

Movement 12: Now the robot must advance supported by the *near wheels* and the arm's end effector until the *far wheels* (raised wheels) exceed *Edge 2* by a safety distance d_s. It is expected that, during the advance, the robot maintains the elevation of the *far wheels* reached in the previous stage (height greater than ${}^{s1}z_{1b2}$ and/or ${}^{s1}z_{2b2}$). To achieve this, as the robot advances Δx at time intervals Δt, its inclination will be with a constant α_c and ϕ_c changing continuously according to (23), if the robot advances supported by the front wheels.

$$\phi_c = \tan^{-1}\left(\frac{\dfrac{{}^M z_{c1} - {}^M z_{l1}}{{}^c x_{l1} - {}^c x_{c1}}}{\sqrt{1 - \left(\dfrac{{}^M z_{c1} - {}^M z_{l1}}{{}^c x_{l1} - {}^c x_{c1}}\right)^2}}\right) \tag{23}$$

In this case, l_1 and c_1 correspond to a *far* and *near wheel* respectively, belonging to the same side, with contact points having coordinates ${}^M P_{l1}({}^M x_{l1}, {}^M y_{l1}, {}^M z_{l1},)$ and ${}^M P_{c1}({}^M x_{c1}, {}^M y_{c1}, {}^M z_{c1})$ in the $X_M Y_M Z_M$ frame, and coordinates ${}^c P_{l1}({}^c x_{l1}, {}^c y_{l1}, {}^c z_{l1})$ and ${}^c P_{c1}({}^c x_{c1}, {}^c y_{c1}, {}^c z_{c1})$ in the $X_c Y_c Z_c$ frame. On the other hand,

https://doi.org/10.1017/S0263574725000542 Published online by Cambridge University Press

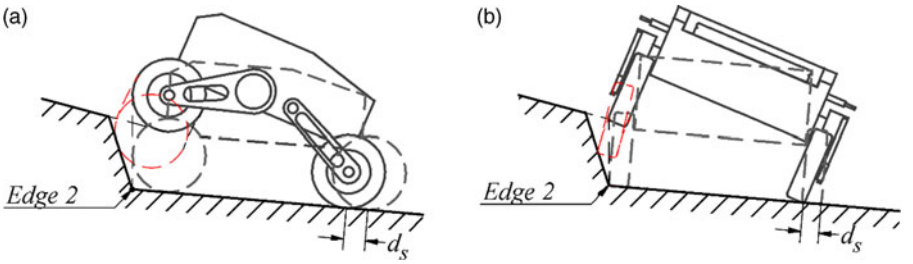


Figure 17. *Safety distance in descent with: (a) rear wheels; (b) lateral wheels.*

if during the advance, the robot is supported on lateral wheels, the angle ϕ_c remains constant while α_c changes continuously according to (24). In this case, the *far wheel* l_1 and the *near* wheel c_1 must both belong to either the front of the robot (wheels 1 and 2) or the rear of the robot (wheels 3 and 4).

$$\alpha_c = \tan^{-1}\left(\frac{\dfrac{{}^{M}z_{c1} - {}^{M}z_{l1}}{c\phi_c\,({}^{c}y_{c1} - {}^{c}y_{l1})}}{\sqrt{1 - \left(\dfrac{{}^{M}z_{c1} - {}^{M}z_{l1}}{c\phi_c\,({}^{c}y_{c1} - {}^{c}y_{l1})}\right)^2}}\right) \tag{24}$$

Given ϕ_c and α_c, the position of the robot ${}^{M}O_c$ can be obtained at each instant as well as the extension of the arm's second link d_2 using (32), which will be the necessary action to keep the *far wheels* at the expected height. Then, the coordinates ${}^{M}E_{l1}$ and ${}^{M}E_{l2}$ of the rear vertices of the safety rectangle (vertices 3 and 4, Figure 3) can be found. These coordinates will be used to evaluate if the rear wheels have completely surpassed the *Edge 2* according to (10) (considering γ_{b2} instead of γ_{b1}), plus a safety distance d_s. This distance is $d_s \approx 0$ if the robot is ascending over the obstacle or surpassing trenches. However, in the descent of obstacles, it is necessary to define a sufficient d_s to ensure that, during the subsequent descent of the wheels, they do not collide with the obstacle (see Figure 17). In the case of the descent of rear wheels, d_s is defined by (25), whereas in the descent of lateral wheels, it is defined by (26), where r_r and a_r are the radius and width of the wheels, and (ϕ_{ci}, α_{ci}) are the pitch and roll angles of the robot at the instant when the descent of the *far wheels* begins.

$$d_s = R_r \tan\left(\frac{90^\circ - \phi_{s2}}{2}\right) + x_t - \left(\frac{x_t \cos\phi_{ci} + R_r}{\cos\phi_{s2}}\right) \tag{25}$$

$$d_s = \frac{1}{\cos\phi_{s2}}\left(R_r + \frac{a_r}{2\,|\tan\gamma_{b2}|}\right) + \frac{(y_t + a_r)\,(\cos\alpha_{s2} - \cos\alpha_{ci})}{\cos\alpha_{s2}\,|\tan\gamma_{b2}|} \tag{26}$$

Stage h. Landing

Movement 13: includes the retraction of the second link of the arm until the *far wheels* touch *Surface 2*. In this case, the robot also undergoes a rotation with an instantaneous axis of rotation formed by the contact points of the *near wheels* with the ground, causing a variation in ϕ_c (if the *near wheels* are frontal) or α_c (if the *near wheels* are lateral). Therefore, if the initial position ${}^{M}P_n$ of a *near wheel* from the previous stage is known, its new position can be calculated as variations in ϕ_c or α_c occur over Δt. From this, the real position of the descending far wheels (${}^{M}P_{l1}$ and ${}^{M}P_{l2}$) (wheels l_1 and l_2) in the $X_M Y_M Z_M$ frame can be obtained using (1)–(2). This position, combined with the procedure described in Section 2.3, is used to determine when the *far wheels* make contact with *Surface 2*.

Movements 14 and 15: These two movements sequentially aim to fully retract the second link of the arm and then reposition the arm in front of the robot to continue navigation (similar to *movement 1*).

https://doi.org/10.1017/S0263574725000542 Published online by Cambridge University Press

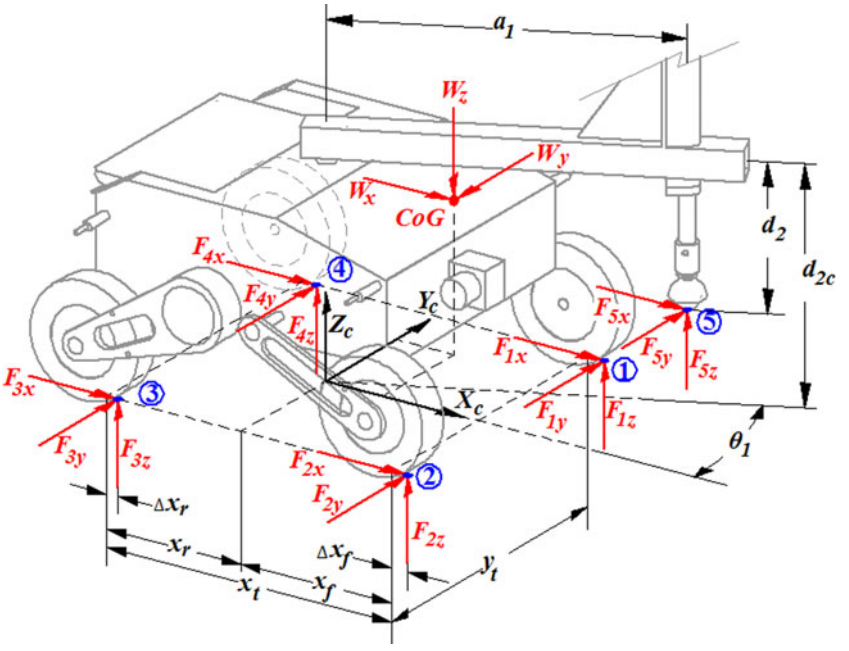


Figure 18. *Reaction forces on wheels of the Lázaro robot.*

4. Tip-over stability analysis

During obstacle traversal, it is essential to prevent the robot from tipping due to changes in inclination. Therefore, the tipping tendency must be studied. This work uses a criterion based on reaction forces [33], which includes the effects of perturbing forces generated by the arm's end effector in contact with the ground. According to this criterion, a four-wheeled robot becomes unstable when the sum of the reaction forces along a tipping axis (an imaginary line connecting two consecutive wheel-ground contact points) approaches zero. A normalized stability index is defined by (27), where F_{mn} represents the sum of the reaction forces from two consecutive wheels (m and n) along the Z_c axis ($F_{mnz} = F_{mz} + F_{nz}$). This index, normalized to the robot's weight (W), ranges from 1 (maximum stability) to 0 (imminent tipping).

$$I_t = \frac{\min\left(F_{12z}, F_{23z}, F_{34z}, F_{14z}\right)}{W/2} \tag{27}$$

However, during the obstacle overcoming process, the robot may be supported on three ground contact points. In this case, the normalized stability index depends on the reaction forces at these three contact points. Thus, if the robot is supported on two wheels, m and n, plus the end effector of the arm (contact 5), the stability index is defined by (28).

$$I_t = \frac{\min\left(F_{mz}, F_{nz}, F_{5z}\right)}{W/2} \tag{28}$$

4.1. Reaction forces with the robot supported on its four wheels

Let ϕ_c and α_c be the roll and pitch angles defining the inclination of the robot, respectively. The position of the center of gravity and the weight vector (both defined according to the $X_cY_cZ_c$ frame) can be obtained for any inclination or arm position through (29) and (30), respectively (Figure 18), where *a, b, c* and *d* are constants specific to the robot.

https://doi.org/10.1017/S0263574725000542 Published online by Cambridge University Press

$$\begin{bmatrix} W_x \\ W_y \\ W_z \end{bmatrix} = W \begin{bmatrix} \sin\phi_c \\ \cos\phi_c \sin\alpha_c \\ \cos\phi_c \cos\alpha_c \end{bmatrix} \tag{29}$$

$$\begin{bmatrix} x_{cog} \\ y_{cog} \\ z_{cog} \end{bmatrix} = \begin{bmatrix} a + r\cos\theta_1 \\ b + r\sin\theta_1 \\ c\,d_2 + d \end{bmatrix} \tag{30}$$

$$F_{12z} = F_{1z} + F_{2z} = \frac{1}{x_t - \Delta x_r + \Delta x_f}\left[W_z\left(x_r - \Delta x_r + x_{cog}\right) + W_x z_{cog} - F_{5z}\left(x_r - \Delta x_r + a_1 c\theta_1\right) + F_{5x}\left(d_2 - d_{2c}\right)\right] \tag{31}$$

$$F_{34z} = F_{3z} + F_{4z} = \frac{1}{x_t - \Delta x_r + \Delta x_f}\left[W_z\left(x_f + \Delta x_f - x_{cog}\right) - W_x z_{cog} + F_{5z}\left(-x_f - \Delta x_f + a_1 c\theta_1\right) - F_{5x}\left(d_2 - d_{2c}\right)\right] \tag{32}$$

$$F_{14z} = F_{1z} + F_{4z} = \frac{1}{y_t}\left[W_z\left(\frac{y_t}{2} + y_{cog}\right) - W_y z_{cog} - F_{5z}\left(\frac{y_t}{2} + a_1 s\theta_1\right) + F_{5y}\left(d_2 - d_{2c}\right)\right] \tag{33}$$

$$F_{23z} = F_{2z} + F_{3z} = \frac{1}{y_t}\left[W_z\left(\frac{y_t}{2} - y_{cog}\right) + W_y z_{cog} - F_{5z}\left(\frac{y_t}{2} - a_1 s\theta_1\right) - F_{5y}\left(d_2 - d_{2c}\right)\right] \tag{34}$$

Now, to find the sum of reaction forces F_{mn} on each tipping axis, the static equilibrium moment summation is used considering that the robot and its arm move at low speeds, obtaining the F_{mn} corresponding to the four tipping axes (1–2, 3–4, 1–4, and 2–3), measured on the Z_c axis, which are expressed from (31) to (34).

4.2. Reaction forces with the robot supported on three points

During obstacle traversal, the robot will be supported on three points at certain moments: two consecutive wheels and the end effector of the arm. In this case, it is necessary to determine the reaction forces at these three points, presenting four possible scenarios:

(a) The front wheels are lifted ($F_{1z} + F_{2z} = 0$)**:** the reaction forces on the wheels touching the ground (wheels 3 and 4) can be determined from (33) and (34), considering that $F_{1z} = 0$ and $F_{2z} = 0$. The normal reaction force F_5 at the end effector is obtained through (35), knowing that ϕ_{si} and α_{si} correspond to the tilt angles of the surface i that the end effector of the arm is touching.

(b) The rear wheels are lifted ($F_{3z} + F_{4z} = 0$)**:** the reaction forces on the front wheels (1 and 2) are also obtained from (33) and (34), knowing that $F_{3z} = 0$ and $F_{4z} = 0$. F_5 is obtained through (36).

(c) The left-side lateral wheels are lifted ($F_{1z} + F_{4z} = 0$)**:** the reaction forces on the right-side wheels (2 and 3) are obtained from (31) and (32), knowing that $F_{1z} = 0$ and $F_{4z} = 0$. F_5 is obtained through (37).

(d) The right-side lateral wheels are lifted ($F_{2z} + F_{3z} = 0$)**:** the reaction forces on the left-side wheels (1 and 4) are also obtained from (31) and (32), knowing that $F_{2z} = 0$ and $F_{3z} = 0$. F_5 is obtained through (38).

In any case, the component F_{5z} in (28) is required, which can be obtained from (39)

$$F_5 = \left[W_z\left(x_r - \Delta x_r + x_{cog}\right) + mW_x z_{cog}\right] / \left[\left(x_r - \Delta x_r + a_1 c\theta_1\right)\left(s\phi_c c\alpha_c s\phi_{si} c\alpha_{si} + s\alpha_c s\alpha_{si} + c\phi_c c\alpha_c c\phi_{si} c\alpha_{si}\right) - \left(c\phi_c s\phi_{si} c\alpha_{si} - s\phi_c c\phi_{si} c\alpha_{si}\right)\left(d_2 - d_{2c}\right)\right] \tag{35}$$

$$F_5 = \left[W_z\left(x_f + \Delta x_f - x_{cog}\right) - W_x z_{cog}\right] / \left[\left(x_f + \Delta x_f - a_1 c\theta_1\right)\left(s\phi_c c\alpha_c s\phi_{si} c\alpha_{si} + s\alpha_c s\alpha_{si} + c\phi_c c\alpha_c c\phi_{si} c\alpha_{si}\right) + \left(c\phi_c s\phi_{si} c\alpha_{si} - s\phi_c c\phi_{si} c\alpha_{si}\right)\left(d_2 - d_{2c}\right)\right] \tag{36}$$

$$F_5 = \left[W_z\left(\frac{y_t}{2} + y_{cog}\right) - W_y z_{cog}\right] / \left[\left(\frac{y_t}{2} + a_1 s\theta_1\right)\left(s\phi_c c\alpha_c s\phi_{si} c\alpha_{si} + s\alpha_c s\alpha_{si} + c\phi_c c\alpha_c c\phi_{si} c\alpha_{si}\right) - \left(s\phi_c s\alpha_c s\phi_{si} c\alpha_{si} - c\alpha_c s\alpha_{si} + c\phi_c s\alpha_c c\phi_{si} c\alpha_{si}\right)\left(d_2 - d_{2c}\right)\right] \tag{37}$$

https://doi.org/10.1017/S0263574725000542 Published online by Cambridge University Press

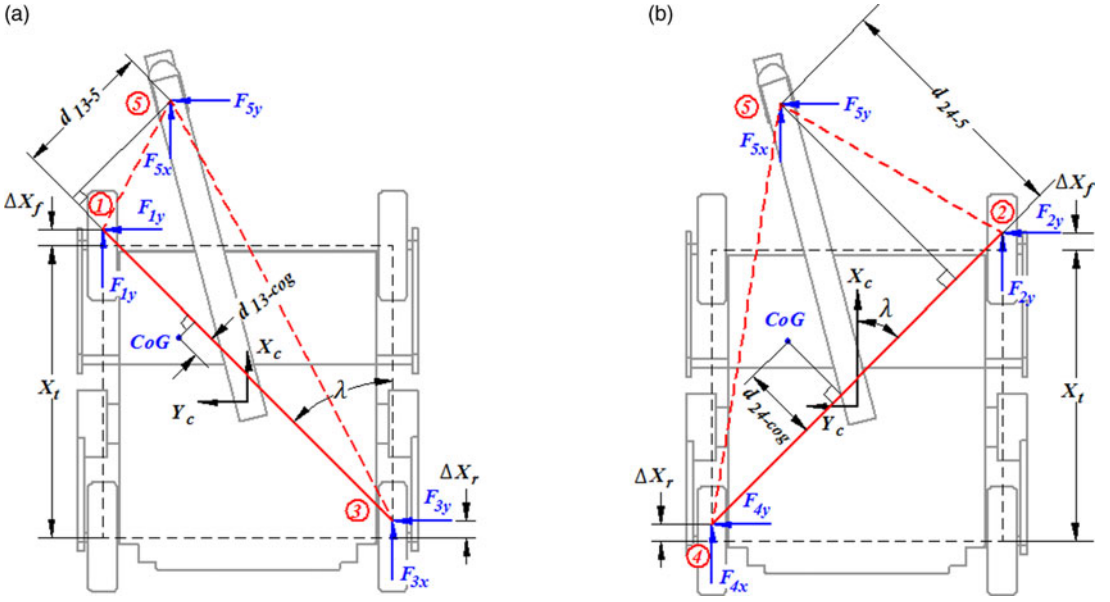


Figure 19. *Top view of the Lázaro robot showing rotation axes: (a) 1–3; (b) 2–4.*

$$F_5 = \left[W_z\left(\frac{y_t}{2} - y_{cog}\right) + W_y z_{cog}\right] / \left[\left(\frac{y_t}{2} - a_1 s\theta_1\right)\ (s\phi_c c\alpha_c s\phi_{si} c\alpha_{si} + s\alpha_c s\alpha_{si} + c\phi_c c\alpha_c c\phi_{si} c\alpha_{si}) + (s\phi_c s\alpha_c s\phi_{si} c\alpha_{si} - c\alpha_c s\alpha_{si} + c\phi_c s\alpha_c c\phi_{si} c\alpha_{si})\ (d_2 - d_{2c})\right] \tag{38}$$

$$F_{5z} = F_5\ (s\phi_c c\alpha_c s\phi_{si} c\alpha_{si} + s\alpha_c s\alpha_{si} + c\phi_c c\alpha_c c\phi_{si} c\alpha_{si}) \tag{39}$$

$$F_5 = \left[\left(W_y c\lambda + W_x s\lambda\right) Z_{cog} - S_{cog} d_{13-cog} W_z\right] / \{(d_2 - d_{2c})\ [c\lambda\ (s\phi_c s\alpha_c s\phi_{si} c\alpha_{si} - c\alpha_c s\alpha_{si} + c\phi_c s\alpha_c c\phi_{si} c\alpha_{si}) - s\lambda\ (c\phi_c s\phi_{si} c\alpha_{si} - s\phi_c c\phi_{si} c\alpha_{si})] - S_5 d_{13-5}\ (s\phi_c c\alpha_c s\phi_{si} c\alpha_{si} + s\alpha_c s\alpha_{si} + c\phi_c c\alpha_c c\phi_{si} c\alpha_{si})\} \tag{40}$$

$$F_5 = \left[\left(W_y c\lambda - W_x s\lambda\right) Z_{cog} - S_{cog} d_{24-cog} W_z\right] / \{(d_2 - d_{2c})\ [c\lambda\ (s\phi_c s\alpha_c s\phi_{si} c\alpha_{si} - c\alpha_c s\alpha_{si} + c\phi_c s\alpha_c c\phi_{si} c\alpha_{si}) + s\lambda\ (c\phi_c s\phi_{si} c\alpha_{si} - s\phi_c c\phi_{si} c\alpha_{si})] - S_5 d_{24-5}\ (s\phi_c c\alpha_c s\phi_{si} c\alpha_{si} + s\alpha_c s\alpha_{si} + c\phi_c c\alpha_c c\phi_{si} c\alpha_{si})\} \tag{41}$$

4.3. Reaction forces during rotation on two diagonal wheels

Rotation on diagonal wheels occurs as a result of the COG position and can be controlled by the action of the end effector of the arm ($F_5 > 0$), as would happen in *movements 7* and *11*; or it could be spontaneous with $F_5 = 0$ if it occurs in *movements 8, 9,* or *10*. The equations that allow quantifying the reaction forces for two specific cases are described below.

Rotation on wheels 1-3: If the rotation is regulated by the action of the end effector of the arm ($F_5 > 0$), the magnitude of the force F_5 on the effector is obtained from (40), where λ is the angle between the 1–3 axis and the X_c axis, d_{13-cog} and d_{13-5} are the distances defined in the $X_c Y_c$ plane, from the 1–3 axis to the COG and to the contact point of the end effector with the ground (point 5) respectively (Figure 19a); S_{cog} and S_5 take the values given by:

https://doi.org/10.1017/S0263574725000542 Published online by Cambridge University Press

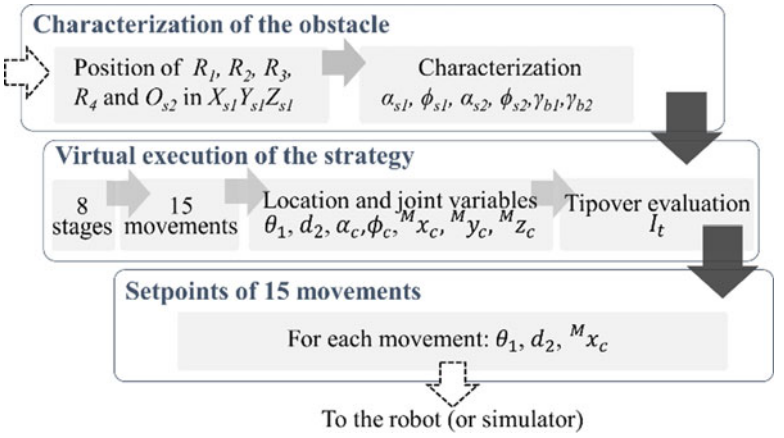


Figure 20. *Planner developed to implement the strategy.*

$$S_{cog} = \begin{cases} 1 & \text{COG is to left of the axis} \\ 0 & \text{COG is on the axis} \\ -1 & \text{COG is to right of the axis} \end{cases} \tag{42}$$

$$S_5 = \begin{cases} 1 & \text{Point 5 is to left of the axis} \\ 0 & \text{Point 5 is on the axis} \\ -1 & \text{Point 5 is to right of the axis} \end{cases} \tag{43}$$

Then, the reaction forces can be calculated: on wheel 1 (F_{1z}) through (31) (knowing that $F_{2z} = 0$); and on wheel 3 (F_{3z}) through (32) (setting $F_{4z} = 0$).

Rotation on wheels 2-4: In this case, if the rotation is regulated by the action of the end effector of the arm ($F_5 > 0$), the magnitude of the force F_5 is obtained from (41), where λ is the angle between the 2–4 axis and the X_c axis, d_{24-cog} and d_{24-5} are the distances defined in the X_cY_c plane, from the 2–4 axis to the COG and to the contact point of the end effector with the ground (point 5) respectively (Figure 19b). From there, the reaction forces are calculated: on wheel 2 (F_{2z}) through (31) (knowing that $F_{1z} = 0$); and on wheel 4 (F_{4z}) through (32) (with $F_{3z} = 0$).

5. Validation of the overcoming strategy

5.1. Simulations

The obstacle-overcoming strategy was implemented in a "planner" program (Figure 20), which performs three main operations: First, based on external information (Localization of R_1, R_2, R_3, R_4, O_{s2}), the obstacle is characterized to define its surfaces and edges and obtain geometric information (α_{s1}, ϕ_{s1}, α_{s2}, ϕ_{s2}, γ_{b1}, γ_{b2}). Second, the overcoming process is computationally emulated through the entire procedure described in Section 3, consisting of 8 stages translating into 15 movements. For each movement, the robot's position and the joint variables' magnitudes are defined at each time instant. Finally, the program generates the sequential commands for the robot to execute each of the 15 movements, including the robot's displacements and the arm's positions (defined by θ_c and d_2).

A model of the Lázaro robot was implemented in MSC. ADAMS dynamic simulation software [34]. Additionally, a control system was developed in SIMULINK to manage the robot's actuators. The SIMULINK system receives *setpoints* from the planner and real-time variables from MSC. ADAMS generates control actions which are then executed by the robot in ADAMS. Using this setup, six

https://doi.org/10.1017/S0263574725000542 Published online by Cambridge University Press

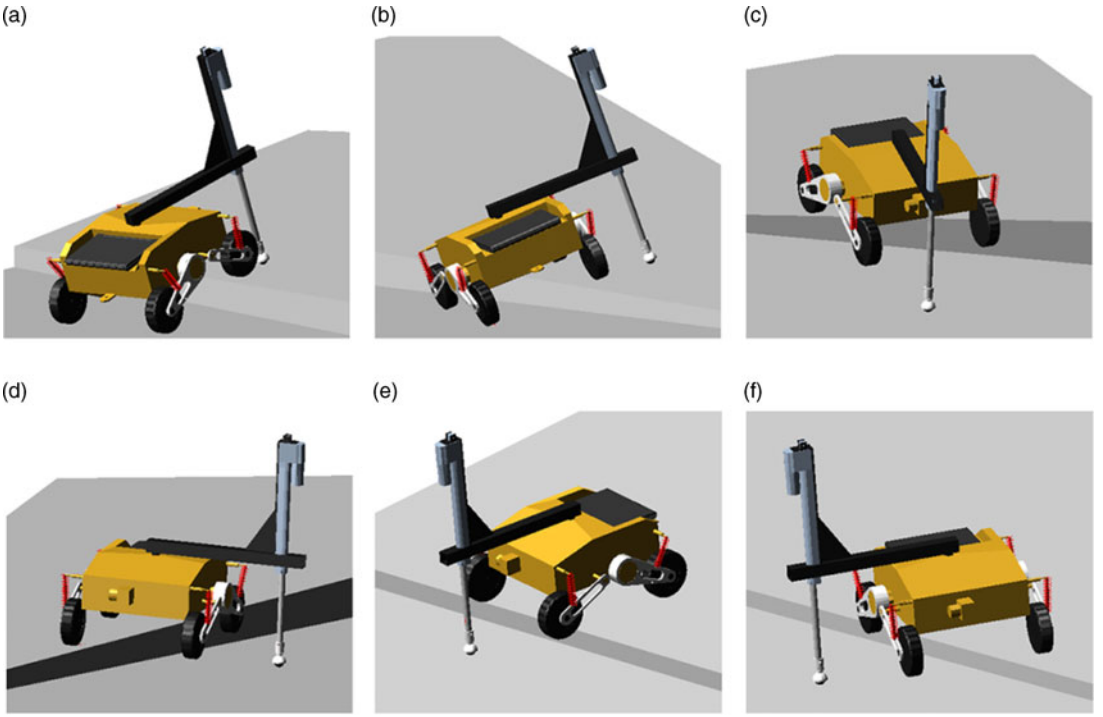


Figure 21. *Simulations carried out in MSC. ADAMS for obstacle overcoming.*

Table 2. *Geometry of obstacles for 6 simulations.*

Simulation	Description	ϕ_{s1} (°)	α_{s1} (°)	ϕ_{s2} (°)	α_{s2} (°)	γ_{b1}(°)
a	Front rise	−5.0	0.0	−9.7	−2.6	74.9
b	Lateral rise	0.0	−5.0	−3.6	−9.3	20.9
c	Front descent	0.0	5.0	8.7	5.0	60.1
d	Lateral descent	7.7	0.0	7.5	−4.3	150.2
e	Front ditch	10.0	0.0	10.0	0.0	100.2
f	Lateral ditch	0.0	10.0	0.0	10.0	25.3

simulations were conducted (Figure 21) to represent various types of obstacles. Table 2 summarizes the information for these obstacles. The results from these simulations were compared to those obtained from the planner. Figure 22, for simulation C, shows a comparison of the position parameters (${}^{M}x_c$, ${}^{M}y_c$, ${}^{M}z_c$, d_2) and orientation (ϕ_c,α_c,θ_1) from both the planner and the simulation.

Firstly, while there is absolute equivalence between these parameters, the planner does not accurately quantify the execution time of the obstacle overcoming strategy. The planner estimates the strategy's completion in 60 s, whereas the simulation estimates it in 80s due to differing standard movement speeds and the planner's lack of consideration for speed variations at the start and stop of each movement. If these results are plotted as a function of their magnitudes at the beginning and end of each movement (15 in total), Figure 23 demonstrates total correspondence between the planner and the simulation. This ensures that the planner's generated actions (setpoints) are appropriate and allow the robot to efficiently overcome an obstacle.

To complement these results, Table 3 provides a statistical comparison between the planner and each simulation, including the mean error ($\overline{\mu}$), standard deviation (σ), and mean absolute percentage error (*MAPE*) for variables ϕ_c,α_c,θ_1, and d_2. Analyzing $\overline{\mu}$ and σ confirms the planner's high reliability

https://doi.org/10.1017/S0263574725000542 Published online by Cambridge University Press

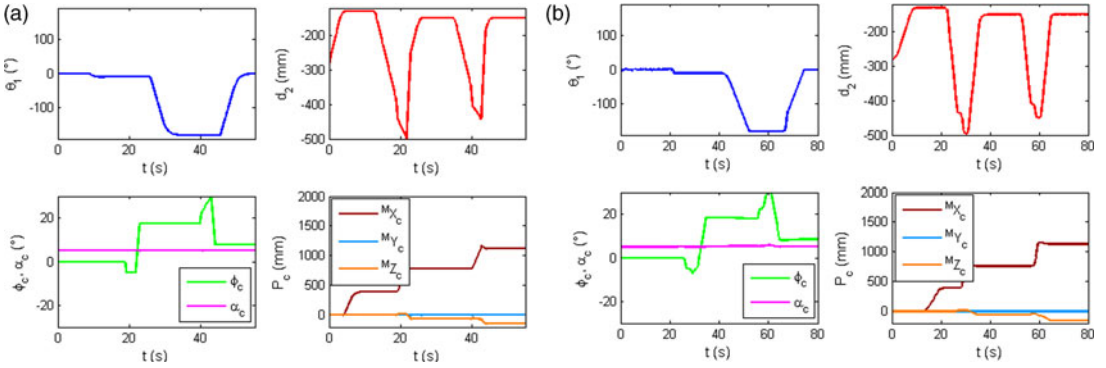


Figure 22. *Position and orientation parameters of the robot obtained in Simulation C: (a) Planner; (b) Simulation.*

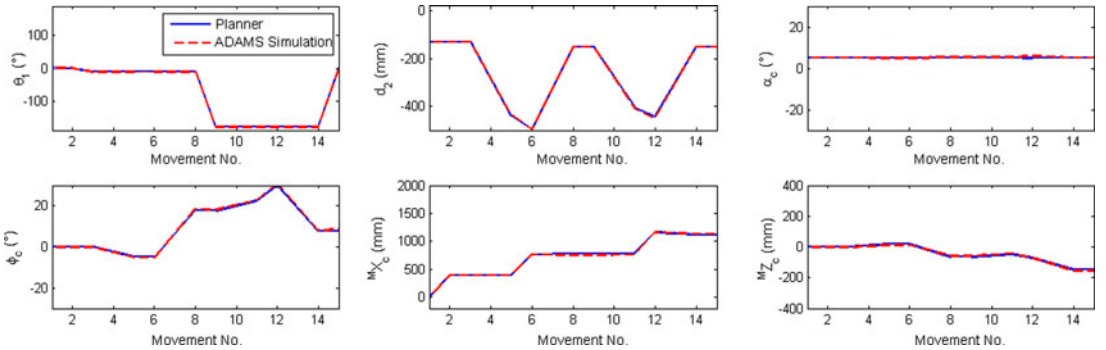


Figure 23. *Comparison of position and orientation parameters of the robot, obtained with the planner and Simulation C.*

Table 3. *Statistical comparison between planner and simulations for $\boldsymbol{\theta}_1$, d_2, $\boldsymbol{\alpha}_c$ and $\boldsymbol{\phi}_c$.*

	$\boldsymbol{\theta}_1$			d_2			$\boldsymbol{\alpha}_c$			$\boldsymbol{\phi}_c$		
Sim.	$\overline{\mu}$ (°)	σ (°)	*MAPE* (%)	$\overline{\mu}$ (mm)	σ (mm)	*MAPE* (%)	$\overline{\mu}$ (°)	σ (°)	*MAPE* (%)	$\overline{\mu}$ (°)	σ (°)	*MAPE* (%)
a	0.0	0.3	1.2	−0.2	1.1	0.2	−0.1	0.2	5.0	0.1	0.3	5.2
b	0.0	0.3	0.3	0.0	0.1	0.0	0.1	0.2	2.8	0.3	0,3	4,6
c	0.2	0.2	1.6	−0.8	2.9	0.4	0.2	0.3	4.1	0.3	0.5	5.0
d	0.0	0.3	0.3	−0.1	0.1	0.0	0.0	0.1	1.4	−0.4	0.2	4.8
e	0.1	0.2	0.2	0.2	0.5	0.1	0.1	0.1	2.0	−0.3	0.2	3.4
f	0.0	0.3	0.3	0.0	0.1	0.0	0.0	0.1	1.5	−0.4	0.2	4.6

due to their low magnitudes. This is further evidenced by the *MAPE*, which has a maximum value of 5.2%, indicating high precision in the planner's forecasts. Figure 24 compares the results for simulation C, showing total correspondence between the planner and simulation for reaction forces and stability index I_t. Additionally, Tables 4 and 5 present statistical comparisons of these variables for the six simulations, showing that $\overline{\mu}$ and σ are very low compared to the forces' magnitudes, which reach up to 175 N. The maximum *MAPE* in this comparison is 3.3% for forces and 4.7% for I_t, demonstrating the high precision of the planner's equations.

Finally, the effectiveness of the fuzzy inference system that positions the first joint of the arm ($\theta_{1\,sp}$) to improve tip-over stability was studied. Figure 24 shows the stability index I_t (last graph) during the

https://doi.org/10.1017/S0263574725000542 Published online by Cambridge University Press

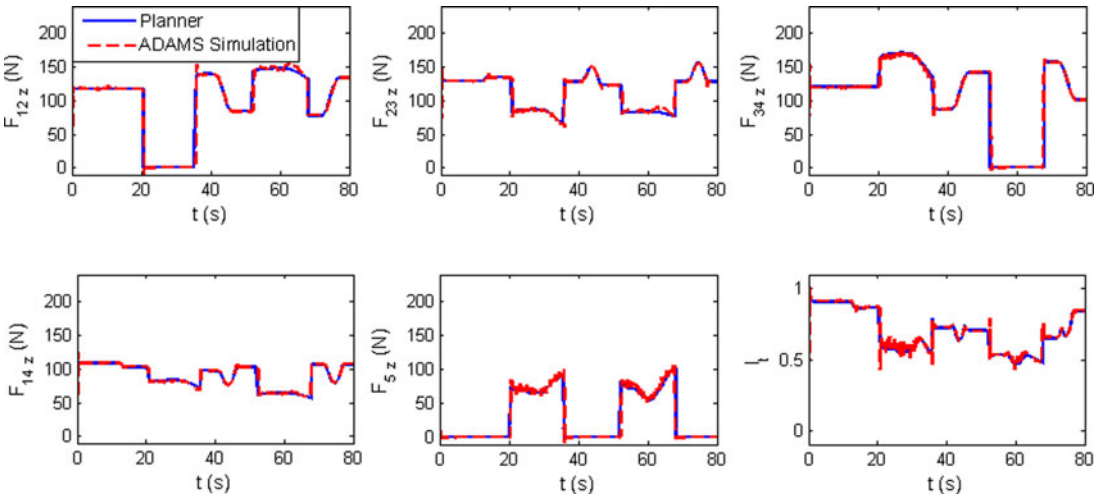


Figure 24. *Comparison of F_{nmz} and I_t obtained with the planner and the simulation.*

Table 4. *Statistical comparison between planner and simulations for forces F_{nmz}.*

	F_{12z}			F_{23z}			F_{34z}			F_{14z}		
Sim.	$\overline{\mu}$ (N)	σ (N)	*MAPE* (%)	$\overline{\mu}$ (N)	σ (N)	*MAPE* (%)	$\overline{\mu}$ (N)	σ (N)	*MAPE* (%)	$\overline{\mu}$ (N)	σ (N)	*MAPE* (%)
a	0.5	6.7	2.4	−0.1	5.2	2.0	−0.4	11.6	1.1	0.1	6.0	1.7
b	0.4	4.8	1.9	2.4	11.0	2.3	−0.9	8.3	3.3	−2.8	12.4	3.3
c	−0.8	9.2	1.4	−0.7	7.0	1.2	0.1	10.3	1.1	0.0	5.6	1.5
d	−0.3	6.7	1.8	1.7	9.8	2.2	−1.0	6.0	2.2	−3.0	9.7	3.2
e	−0.4	9.1	1.1	−0.1	6.4	1.0	0.3	9.8	0.9	−0.1	5.4	1.0
f	−0.1	6.5	1.9	−1.8	11.8	2.3	−1.4	7.1	2.2	0.4	9.0	2.2

Table 5. *Statistical comparison between planner and simulations for I_t.*

	I_t		
Sim.	$\overline{\mu}$	σ	*MAPE*(%)
a	0.0	0.0	3.1
b	0.0	0.0	3.4
c	0.0	0.1	2.0
d	0.0	0.1	4.7
e	0.0	0.0	1.2
f	0.0	0.0	2.3

obstacle overcoming process. It was observed that for all simulations, $I_t > 0.5$ for obstacles near the height limit for Lázaro, 140 mm, due to the dimensions of the second link of the arm defining the limits of d_2 ($-432.5 \leq d_2 \leq -132.5$ mm). With these I_t magnitudes, the robot is guaranteed not to tip over. Then, the lowest I_t values occur when $F_{5z} > 0$, meaning the robot supports itself with the arm's end effector while the first joint is oriented according to $\theta_{1\,sp}$. Other simulations without the fuzzy system, positioning the arm with θ_1 perpendicular to the obstacle, showed $I_t > 0.06$ at the same instant, implying an imminent rollover risk. This comparison confirmed the fuzzy system's effectiveness in enhancing the robot's stability during obstacle overcoming.

https://doi.org/10.1017/S0263574725000542 Published online by Cambridge University Press

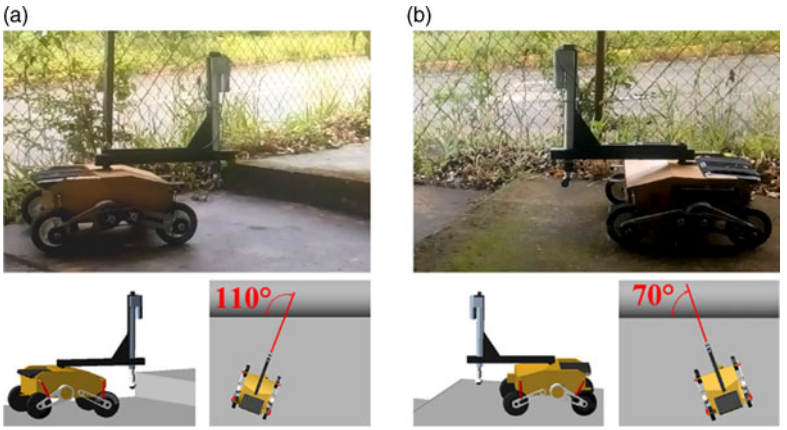


Figure 25. *Implementation of the strategy on the Lázaro robot to overcome obstacles: (a) Test 1: ascent with* γ_{b1}*=110°; (b) Test 2: descent with* γ_{b1}*=70°.*

5.2. Implementation on Lázaro robot

In order for the robot to execute the strategy autonomously, an additional system scans the environment (using a LiDAR), detects the presence of obstacles, characterizes them, and extracts the required dimensional features. Subsequently, the planner is activated, which is fed with this data to obtain the *setpoints* for each movement. These *setpoints* are ultimately delivered to a behavior responsible for commanding the execution of the developed strategy to overcome the obstacle, through a control system that takes these *setpoints* and controls the actuators in a closed loop, continuously fed with data collected by the sensors installed on the robot to measure the variables: θ_1, d_2, ϕ_c and ${}^{M}X_c$.

Preliminary tests on the Lázaro robot verified its capability to overcome obstacles using the developed strategy. The robot was positioned on obstacles with $\gamma_{b1} \neq 90°$ (Test 1: $\gamma_{b1} = 110°$, Test 2: $\gamma_{b1} = 70°$) and a maximum height of 140 mm (Figure 25). Dimensional data from each test were input into the MATLAB planner to obtain s*etpoints* for each movement, which were then delivered to the robot for executing the strategy. Figure 26 shows the stages followed during Test 1 to climb a step, and Figure 27 shows the process for Test 2 to descend a step. Variables measured by the robot's sensors θ_1, d_2, ϕ_c and ${}^{M}X_c$; Figure 28) were compared between real tests and simulations with MSC. ADAMS. The sequences and magnitudes were found to be consistent, validating that the process developed through equations and simulations corresponds to the actual execution of the strategy by the robot.

Finally, it was observed that the strategy's execution time differs between simulation and real implementation: in simulation, the robot overcomes the obstacle in approximately 80 s, while in reality, it takes about 120 s on average. This difference does not invalidate the strategy's effectiveness; it indicates that the robot executes the stages more slowly in reality, considering factors not quantifiable in the simulation, such as sensor data acquisition, communication delays between the robot and a remote PC, processing time, and actuator dynamic response. Despite these factors, the robot successfully overcomes obstacles according to the control setpoints provided by the planner.

6. Final considerations

At this point, it is essential to analyze the requirements for the robot to undertake the obstacle overcoming strategy. Prior knowledge of the obstacle is vital, simplified in this work through five points (R_1, R_2, R_3, R_4, O_{s2}) for complete characterization (edges and surfaces). Other methods include LiDAR [26] or stereo cameras [35]. Characterization is crucial for this deliberative strategy, where all 15 movements are planned in advance. Thus, the mathematical analysis shown in this article is important, as it forms the basis for computational emulation in the planner. Additionally, Eqs. (31)–(41) are relevant, providing sums of the wheel reaction forces with the terrain, useful for roll stability analysis during planning.

https://doi.org/10.1017/S0263574725000542 Published online by Cambridge University Press

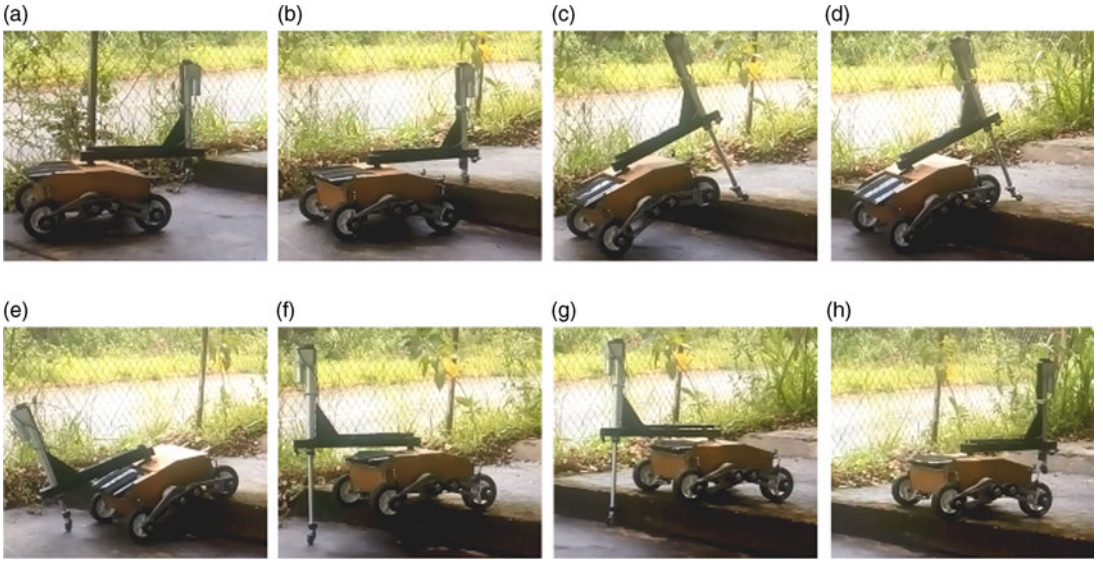


Figure 26. *Process followed by the Lázaro robot when overcoming the obstacle in Test 1.*

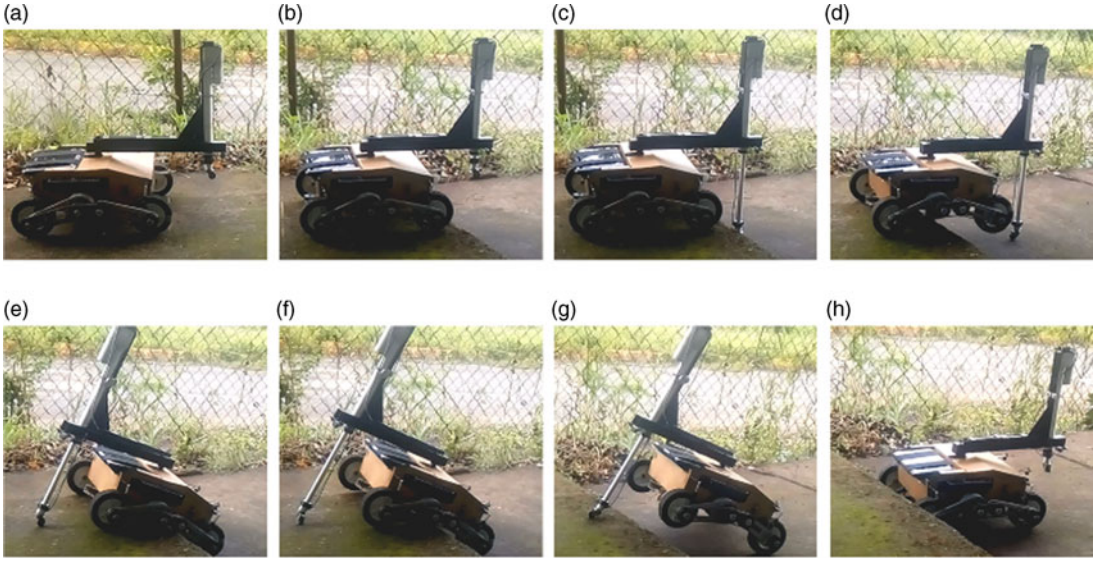


Figure 27. *Process followed by the Lázaro robot when overcoming the obstacle in Test 2.*

This allows for quantitative estimation of tip-over risk before the robot encounters the obstacle, offering an additional safety resource, especially in environments where the robot cannot be recovered after a tip-over that renders it inoperable.

It is important to highlight the increased obstacle-overcoming capability of the Lázaro robot when using the developed strategy. Typically, a wheeled robot can overcome obstacles with a maximum height (H_o) equal to the radius of its wheels (R_r), resulting in $H_o/R_r = 1$. By implementing the strategy, *Lázaro*'s capability increases to $H_o/R_r = 1.9$, which is competitive compared to other robots: *Spirit* and *Opportunity* [36] with $H_o/R_r = 1.60$, *Hanzo* [37] with $H_o/R_r = 1.65$, *Q-Whex* [14] with $H_o/R_r = 1.86$, and *TurboQuad* [38] with $H_o/R_r = 1.38$. While there are robots with greater capabilities, such as *Epi.q-1* [39] with $H_o/R_r = 3.60$, Lázaro's ability is limited by the dimensions of the linear actuator in the second arm link. Changing this actuator could further improve its obstacle-overcoming capability.

https://doi.org/10.1017/S0263574725000542 Published online by Cambridge University Press

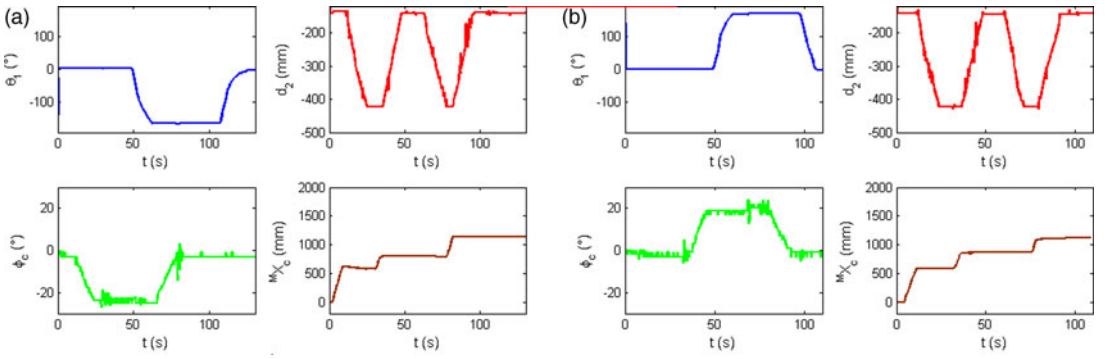


Figure 28. *Parameters of position and orientation of the robot obtained in: (a) Test 1; (b) Test 2.*



Figure 29. *Geometry of obstacles that can decrease the robot's ability to overcome obstacles.*

Also, it is relevant to note that the measured capability H_o/R_r was estimated considering horizontal surfaces, but it can vary with the obstacle's actual inclination. Simulations and tests showed this capability decreases during ascent or descent with front wheels when large obstacle heights and changes in orientation between ϕ_{s1} and ϕ_{s2} are combined (Figure 29). In such cases, the distance d_2 required may exceed the arm's joint limits. Therefore, each test checks if the robot meets dimensional requirements; if not, the planner issues warnings indicating the strategy's infeasibility. The same occurs when tip-over stability analysis indicates a high risk of tipping over.

Finally, analyzing the strategy's applicability to other robots is crucial. Designed for wheeled mobile robots with an articulated arm and an end-effector for ground contact, this strategy's use might be limited. However, other compatible robots like *HEAP* [29], with a fully rotating arm and a digging scoop, could utilize this strategy. Adapting the strategy requires modifying equations involving arm variables (a_1 and d_2) to fit specific arm characteristics.

7. Conclusions

A strategy was defined that allows mobile robots with wheels and an articulated arm to overcome obstacles located on inclined terrain and positioned obliquely to the robot's trajectory. It consists of a procedure formed by 8 stages and 15 autonomous movements that the robot must follow to achieve obstacle traversal. Two of these movements (in the first joint of the arm) were defined through a fuzzy inference system that, based on the inclination of the two surfaces that make up the obstacle and its position relative to the robot, allows positioning the arm in such a way that the risk of tipping over is reduced, which was studied based on the criterion of reaction forces. Equations were defined to study these forces in all stages of the obstacle traversal process.

On the other hand, the strategy was validated using dynamic simulation and then through implementation tests with the Lázaro robot. These validations confirmed that the proposed models for actions and stability index efficiently predict the obstacle traversal process and the associated risks for which they were designed. Additionally, it was demonstrated that these models provide highly accurate predictions.

Future work includes studying slippage during the obstacle traversal process. Considering that the robot moves on inclined surfaces, slippage may occur during the execution of the strategy, potentially hindering its completion. Additionally, the incorporation of reactive elements during the execution of the strategy will be explored. This could allow for the modification of the traversal process in response to disturbances or significant deviations that may occur during the execution.

https://doi.org/10.1017/S0263574725000542 Published online by Cambridge University Press

Acknowledgements. ChatGPT 4.0 [40] and Copilot [41] were used to improve the translation and writing in English.

Author contribution. Jesús M. García conceived and designed the study and performed the simulations and tests. He also wrote the article. Franklyn Duarte led the study, supervised and revised the manuscript.

Financial support. This work was partially funded by project No. 01-025-2016 from Dean of Research of the National Experimental University of Táchira

Competing interests. The authors declare that no conflicts of interest exist.

References

[1] J. M. García, J. L. Martínez, A. Mandow and A. García-Cerezo, "Slide-Down Prevention for Wheeled Mobile Robots on Slopes," *3rd International Conference on Mechatronics and Robotics Engineering, Paris*, (2017).
[2] X. Xu, W. Wang, G. Su, C. Liu, W. Cai, H. Zhang, Y. Ran, Z. Tan and M. Luo, "Obstacle modeling and structural optimization of four-track twin-rocker rescue robot," *Machines* **10**(365), 1–16 (2022).
[3] Y. Huang, R. Meng, J. Yu, Z. Zhao and X. Zhang, "Practical obstacle-overcoming robot with a heterogeneous sensing system: Design and experiments," *Machines* **10**(289), 1–19 (2022).
[4] P. Boeder and C. Soares, "Mars 2020: Mission, Science Objectives and Build," *Proc. SPIE 11489, Systems Contamination: Prediction, Control, and Performance*, vol. **11489** (2020) pp. 1–17.
[5] M. Kara, "Planetary Rovers on Extreme Terrains: Emergencies and Responses," *Selected Proceedings of the 6th Space Resources Conference* (2024).
[6] A. Candela and D. Wettergreen, "An approach to science and risk-aware planetary rover exploration," *IEEE Rob. Autom. Lett.* **7**(4), 9691–9698 (2022).
[7] K. Iagnemma, A. Rzepniewski, S. Dubowsky and P. Schenker, "Control of robotic vehicles with actively articulated suspensions in rough terrain," *Auton. Robots* **14**(1), 5–16 (2003).
[8] S. Zhang, X. Zhao, W. Su, H. Wu, Z. Dai and Z. Chen, "The Design of Suspension Mechanism and Analysis of Obstacle Ability to Rescue Robots," **In:** *Recent Developments in Mechatronics and Intelligent Robotics. ICMIR 2018. Advances in Intelligent Systems and Computing* (2018).
[9] M. Heverly, J. Matthews, J. Lin, D. Fuller, M. Maimone, J. Biesiadecki and J. Leichty, "Traverse performance characterization for the mars science laboratory rover," *J. Field Rob.* **30**(6), 835–846 (2013).
[10] M. Morita, T. Nishida, Y. Arita, M. Shige-eda, E. di Maria, R. Gallone and N. I. Giannoccaro, "Development of robot for 3D measurement of forest environment," *J. Rob. Mechatron.* **30**(1), 145–154 (2018).
[11] C. Cosenza, V. Niola, S. Pagano and S. Savino, "Theoretical study on a modified rocker-bogie suspension for robotic rovers," *Robotica* **41**(10), 2915–2940 (2023).
[12] Z. Song, Z. Luo, G. Wei and J. Shang, "Design and analysis of a six-wheeled companion robot with mechanical obstacle-overcoming adaptivity," *Mech. Sci.* **12**(2), 1115–1136 (2021).
[13] D. Son, J. Shin, Y. Kim and T. Seo, "LEVO: Mobile robotic platform using wheel mode switching primitives," *Int. J. Precis. Eng. Manuf.* **23**, 1291–1300 (2022).
[14] G. Zhang, S. Ma, J. Liu, X. Zeng, L. Kong and Y. L., "Q-Whex: A simple and highly mobile quasi-wheeled hexapod robot," *J. Field Rob.* **40**(6), 1444–1459 (2023).
[15] C. Zheng, S. Sane, K. Lee, V. Kalyanram and K. Lee, "α-WaLTR: Aadaptive wheel-and-leg transformable robot for versatile multiterrain locomotion," *IEEE Trans. Rob.* **39**(2), 941–958 (2023).
[16] Z. Wei, G. Song, H. Sun, Q. Qi, S. Liu and G. Qiao, "Step-Climbing Maneuver for Transleg in the Wheeled Mode," *18th International Conference on Advanced Robotics (ICAR), Hong Kong* (2017).
[17] J. Zhao, Z. Zhang, S. Liu, Y. Tao and Y. Liu, "Design and research of an articulated tracked firefighting robot," *Ah S Sens.* **22**(5086), 1–24 (2022).
[18] X. Gao, D. Cui, W. Guo, Y. Mu and B. Li, "Dynamics and stability analysis on stairs climbing of wheel-track mobile robot," *Int. J. Adv. Rob. Syst.* **14**(4), 1–13 (2017).
[19] F. Cordes, F. Kirchner and A. Babu, "Design and field testing of a rover with an actively articulated suspension system in a mars analogue terrain," *J. Field Rob.* **35**(7), 1149–1181 (2018).
[20] V. Klemm, A. Morra, C. Salzmann, F. Tschopp, K. Bodie, L. Gulich, N. Küng, D. Mannhart, C. Pfister, M. Vierneisel, F. Weber, R. Deuber and R. Siegwart, "Ascento: A Two-Wheeled Jumping Robot," *2019 International Conference on Robotics and Automation, Montreal* (2019).
[21] D. Lu, E. Dong, C. Liu, M. Xu and J. Yang, "Design and Development of a Leg-Wheel Hybrid Robot 'HyTRo-I'," *2013 IEEE/RSJ International Conference on Intelligent Robots and Systems (IROS), Tokyo* (2013).
[22] L. Shang, H. Wang, H. Si, Y. Li and T. Pan, "Investigating the obstacle climbing ability of a coal mine search-and-rescue robot with a hydraulic mechanism," *Appl. Sci.* **12**(20), 1–14 (2022).
[23] T. Fujita, T. Sasaki and Y. Tsuchiya, "Hybrid Motions by a Quadruped Tracked Mobile Robot," *2015 IEEE International Symposium on Safety, Security, and Rescue Robotics (SSRR), West Lafayette* (2015).
[24] X. Gao, X. Guan, Y. Yang and J. Zhang, "Design and ground performance evaluation of a multi-joint wheel-track composite mobile robot for enhanced terrain adaptability," *Appl. Sci.* **13**(12), 1–19 (2023).

https://doi.org/10.1017/S0263574725000542 Published online by Cambridge University Press

[25] T. Guo, J. Liu, H. Liang, Y. Zhang, W. Chen, X. Xia, M. Wang and Z. Wang, "Design and dynamic analysis of jumping wheel-legged robot in complex terrain environment," *Front. Neurorob.* **16**(1066714), 1–17 (2022).
[26] J. Serón, J. L. Martínez, A. Mandow, A. García-Cerezo, J. Morales, A. Reina and J. García, "Terrace Climbing of the Alacrane Mobile Robot with Cooperation of Its Onboard Arm," *12th IEEE International Workshop On Advanced Motion Control, Sarajevo* (2012).
[27] J. M. García, I. Medina, J. L. Martínez, A. García-Cerezo, A. Linares and C. Porras, "Lázaro: Robot Móvil dotado de Brazo para Contacto con el Suelo," *Revista Iberoamericana Autom. Inf. Ind.* **14**(2), 174–183 (2017).
[28] J. M. García, J. L. Martínez, A. Mandow and A. García-Cerezo, "Caster-leg aided maneuver for negotiating surface discontinuities with a wheeled skid-steer mobile robot," *Rob. Auton. Syst.* **91**, 25–37 (2017).
[29] E. Jelavic and M. Hutter, "Whole-Body Motion Planning for Walking Excavators," *2019 IEEE/RSJ International Conference on Intelligent Robots and Systems (IROS), Macau* (2019).
[30] J. Morales, J. Martínez, A. Mandow, J. Serón, A. García-Cerezo and A. Pequeño-Boter, "Center of Gravity Estimation and Control for a Field Mobile Robot with a Heavy Manipulator," *IEEE International Conference on Mechatronics, Málaga* (2009).
[31] A. Diaz-Calderon and A. Kelly, "Development of a Terrain Adaptive Stability Prediction System for Mass Articulating Mobile Robots," **In:** *Field and Service Robotics* (Springer Berlin Heidelberg, Berlín, 2006) pp. 343–354.
[32] J. M. García, A. Gíl and E. Sánchez, "Desarrollo de una arquitectura de software para el robot móvil Lázaro," *Ingeniare* **26**(3), 376–390 (2018).
[33] J. García, J. L. Martínez, A. Mandow and A. García-Cerezo, "Steerability Analysis on Slopes of a Mobile Robot with a Ground Contact Arm," *23rd Mediterranean Conference on Control and Automation, Torremolinos, Spain* (2015).
[34] A. Grazioso, A. Ugenti, R. Galati, G. Mantriota and G. Reina, "Modeling and validation of a novel tracked robot via multibody dynamics," *Robotica* **41**(10), 3211–3232 (2023).
[35] C. Sung and P. Y. Kim, "3D terrain reconstruction of construction sites using a stereo camera," *Autom. Constr.* **64**, 65–77 (2016).
[36] R. Lindemann, D. Bickler, B. Harrington, G. Ortiz and C. Voorhees, "Mars exploration rover mobility development," *IEEE Rob. Autom. Mag.* **13**(2), 19–26 (2006).
[37] N. Shiroma, Y. Chiu, Z. Min, I. Kawabuchi and F. Matsuno, "Development and Control of a High Maneuverability Wheeled Robot with Variable-Structure Functionality," *2006 IEEE/RSJ International Conference on Intelligent Robots and Systems, Beijing* (2006).
[38] W. Chen, H. Lin, Y. Lin and P. Lin, "TurboQuad: A novel leg-wheel transformable robot with smooth and fast behavioral transitions," *IEEE Trans. Rob.* **33**(5), 1025–1040 (2017).
[39] G. Quaglia, R. Oderio, L. Bruzzone and R. Razzoli, "A modular approach for a family of ground mobile robots," *Int. J. Adv. Rob. Syst.* **10**(296), 1–11 (2013).
[40] OpenAI, ChatGPT-4 [Large language model] (2023). [En línea]. Available: https://www.openai.com/.
[41] Microsoft, Copilot [AI companion] (2024). [En línea]. Available: https://www.microsoft.com/.

Appendix. Nomenclature utilized in equations

a_r	**Wheel width**
a_1	Horizontal reach of the arm
${}^{C}E_n$	Vertex of an imaginary rectangle that encompasses all the constituent parts of the robot chassis, with position estimated in $X_cY_cZ_c$ frame ($n = 1...4$)
${}^{C}P_n$	Wheel contact point i with the ground, with position estimated in $X_cY_cZ_c$ frame ($n = 1...5$)
${}^{c}x_{En}$, ${}^{c}y_{En}$,0	Coordinates of each vertex of an imaginary rectangle that encompasses all the constituent parts of the robot chassis, estimated in $X_cY_cZ_c$ frame ($n = 1...4$)
${}^{C}x_n$, ${}^{C}y_n$, ${}^{C}z_n$	Coordinates of the wheel contact point n with the ground, estimated in $X_cY_cZ_c$ frame ($n = 1...5$)
d_s	Safety distance
d_{si}	Safety distance in a specific situation i
d_{13-cog}	Distance defined in the X_cY_c plane, from the 1–3 axis to the COG
d_{13-5}	Distance defined in the X_cY_c plane, from the 1–3 axis to the contact point of the end effector
d_2	Joint variable of the second joint of the robot arm
d_{2c}	Magnitude of d_2 when the end effector touches the ground while the robot is on a horizontal surface

https://doi.org/10.1017/S0263574725000542 Published online by Cambridge University Press

d_{24-cog}	Distance defined in the X_cY_c plane, from the 2–4 axis to the COG
d_{24-5}	Distance defined in the X_cY_c plane, from the 2–4 axis to the contact point of the end effector
F_{nz}	Component of the reaction force of a wheel on Z_c axis
F_{mn}	Sum of the reaction forces from two consecutive wheels (m and n)
F_{mnz}	Sum of the reaction forces from two consecutive wheels (m and n) in Z_c axis
H_o	Maximum height of the obstacle that the robot is able to overcome
${}^{H}P_{COG}$	Orthogonal projection of COG on a horizontal plane
${}^{H}P_i$	Orthogonal projection of a point i on a horizontal plane
I_t	Tip-over stability index
O_c	Origin of the $X_cY_cZ_c$ frame
O_{s1}	Origin of the $X_{s1}Y_{s1}Z_{s1}$ frame
O_{s2}	Origin of the $X_{s2}Y_{s2}Z_{s2}$ frame
${}^{M}O_c$	Origin of the $X_cY_cZ_c$ frame, with position estimated in $X_MY_MZ_M$ frame
${}^{M}O_{s2}$	Origin of the $X_{s2}Y_{s2}Z_{s2}$ frame, with position estimated in $X_MY_MZ_M$ frame
${}^{M}P_n$	Point n, with position estimated in $X_MY_MZ_M$ frame
${}^{M}R_3$	Point R_3, with position estimated in $X_MY_MZ_M$ frame
${}^{M}T_c$	Homogeneous transformation matrix of the $X_cY_cZ_c$ frame with respect to the $X_MY_MZ_M$ frame
${}^{\parallel M}\overrightarrow{U}_{Z_{s2}}$	Unit vector of the Z_{s2} axis with respect to a frame parallel to $X_MY_MZ_M$ with the origin at O_{s2}
${}^{M}X_c.$	Robot advance in longitudinal direction estimated in $X_MY_MZ_M$ frame
${}^{M}x_n, {}^{M}y_n, {}^{M}z_n$	Coordinates of n point, estimated in $X_MY_MZ_M$ frame
${}^{M}x_{Oc}, {}^{M}y_{Oc}, {}^{M}z_{Oc}$	Coordinates of O_c point, estimated in $X_MY_MZ_M$ frame
${}^{M}x_{O2}, {}^{M}y_{O2}, {}^{M}z_{O2}$	Coordinates of O_{s2} point, estimated in $X_MY_MZ_M$ frame
${}^{\parallel M}x_{z_{s2}}, {}^{\parallel M}y_{z_{s2}}, {}^{\parallel M}z_{z_{s2}}$	Components of the unit vector ${}^{\parallel M}\overrightarrow{U}_{Z_{s2}}$
t	Time
R_r	Radius of the wheels
R_1	Point defined by the intersection of the $X_{s1}Z_{s1}$ plane with Edge 1
R_2	Any point belonging to Edge 1
R_3	Any point belonging to Edge 3
R_4	Any point belonging to Surface 2
S_{cog}	Sign function defined according to (**42**)
${}^{s1}E_n$	Vertex of an imaginary rectangle that encompasses all the constituent parts of the robot chassis, with position estimated in $X_{s1}Y_{s1}Z_{s1}$ frame ($n = 1...4$)
${}^{s1}O_{s2}$	Point O_{s2} with position estimated in $X_{s1}Y_{s1}Z_{s1}$ frame
${}^{s1}P_i$	Point i with position estimated in $X_{s1}Y_{s1}Z_{s1}$ frame
${}^{s1}R_i$	Point R_i with position estimated in $X_{s1}Y_{s1}Z_{s1}$ frame
${}^{s1}T_M$	Homogeneous transformation matrix of the $X_MY_MZ_M$ frame with respect to the $X_{s1}Y_{s1}Z_{s1}$ frame
${}^{s1}\overrightarrow{U}_{Z_{s2}}$	Unit vector of the Z_{s2} axis with respect to the $X_{s1}Y_{s1}Z_{s1}$ frame
${}^{s1}x_i, {}^{s1}y_i, {}^{s1}z_i$	Coordinates of a point i, estimated in $X_{s1}Y_{s1}Z_{s1}$ frame
${}^{s1}z_{ib2}$	Height of the obstacle measured in front of the front wheel i
${}^{s2}P$	Point with position estimated in $X_{s2}Y_{s2}Z_{s2}$ frame
${}^{s2}T_M$	Homogeneous transformation matrix of the $X_MY_MZ_M$ frame with respect to the $X_{s2}Y_{s2}Z_{s2}$ frame
${}^{s2}x_i, {}^{s2}y_i, {}^{s2}z_i$	Coordinates of a point i, estimated in $X_{s2}Y_{s2}Z_{s2}$ frame
S_5	Sign function defined according to (43)

https://doi.org/10.1017/S0263574725000542 Published online by Cambridge University Press

V_c	Forward speed of the robot in longitudinal direction
V_{d2}	Advancing speed of the second link of the arm
W	Robot's weight
W_x, W_y, W_z	Components of the robot weight vector in the $X_cY_cZ_c$ frame
$X_cY_cZ_c$	Frame attached to the robot
x_{cog}, y_{cog}, z_{cog}	Coordinates of the center of gravity in the $X_cY_cZ_c$ frame
x_f	Horizontal distance from the $X_cY_cZ_c$ frame to the axis of the front wheels
$X_{s1}Y_{s1}Z_{s1}$	Fixed frame attached to Surface 1
$X_{s2}Y_{s2}Z_{s2}$	Fixed frame attached to Surface 2
$X_MY_MZ_M$	Global fixed frame
x_r	Horizontal distance from the $X_cY_cZ_c$ frame to the axis of the rear wheels
x_t	Distance between the front and rear wheels
y_t	Distance between side wheels
α_c	Roll angle of the robot with respect to the $X_MY_MZ_M$ frame
α_{s1}	Roll angle of the $X_{s1}Y_{s1}Z_{s1}$ frame with respect to the $X_MY_MZ_M$ frame
α_{s2}	Roll angle of the $X_{s2}Y_{s2}Z_{s2}$ frame with respect to the $X_MY_MZ_M$ frame
β_i	Maximum slope director angles of Surface i
γ_{b1}	Inclination of the horizontal projection of Edge 1 with respect to the X_M axis
γ_{b2}	Inclination of the horizontal projection of Edge 2 with respect to the X_M axis
Δt	Time variations
Δx	Robot's forward motion in the longitudinal direction
Δx_f	Variation in the position of the front wheel contact points
Δx_r	Variation in the position of the rear wheel contact points
θ_1	Joint variable of the first joint of the robot arm
$\theta_{1\,sp}$	Setpoint in the first joint of the arm obtained by the fuzzy inference system
λ	Angle between the axis defined by two diagonal wheels and the X_c axis
$\overline{\mu}$	Mean error
σ	Standard deviation
ϕ_c	Pitch angle of the robot with respect to the $X_MY_MZ_M$ frame
ϕ_{s1}	Pitch angle of the $X_{s1}Y_{s1}Z_{s1}$ frame with respect to the $X_MY_MZ_M$ frame
ϕ_{s2}	Pitch angle of the $X_{s2}Y_{s2}Z_{s2}$ frame with respect to the $X_MY_MZ_M$ frame

Cite this article: J. M. García and F. Duarte (2025). "Overcoming obstacles with variable geometry and inclination by rolling mobile robots using their arm", Robotica **43**, 1608–1639. https://doi.org/10.1017/S0263574725000542

https://doi.org/10.1017/S0263574725000542 Published online by Cambridge University Press